Report Submitted to	Jason Montgomery, Ph.D. Advanced Energy Systems Division U.S. DOE, National Energy Technology Laboratory 626 Cochrans Mill Road, P.O. Box 10940, Pittsburgh, PA 15236 Phone: (412) 386-4009 Email: Jason.Montgomery@netl.doe.gov
Project Number	DE-FE0031667
Project Title	High Performance SOFCs with a Superior Stability for Reliable and Durable Power Systems
PI Contact Information	Professor Xiao-Dong Zhou Stuller Endowed Chair Department of Chemical Engineering University of Louisiana at Lafayette Lafayette, LA 70503 E-mail: zhou@louisiana.edu
Submitted by	Professor Xiao-Dong Zhou 131 Rex Street Lafayette, LA 70503 E-mail: zhou@louisiana.edu
Submission Date	May 31, 2022
DUNS	11-131-0249
Recipient Organization	Sponsored Programs Office University of South Carolina
Project Period	08/01/2018 – 01/31/2022
Reporting Period End Date	4/30/2022
Report Frequency	Final Report
Signature	

DISCLAIMER* -- The Disclaimer must follow the title page, and must contain the following paragraph:

> "This report was prepared as an account of work sponsored by an agency of the United States Government. Neither the United States Government nor any agency thereof, nor any of their employees, makes any warranty, express or implied, or assumes any legal liability or responsibility for the accuracy, completeness, or usefulness of any information, apparatus, product, or process disclosed, or represents that its use would not infringe privately owned rights. Reference herein to any specific commercial product, process, or service by trade name, trademark, manufacturer, or otherwise does not necessarily constitute or imply its endorsement, recommendation, or favoring by the United States Government or any agency thereof. The views and opinions of authors expressed herein do not necessarily state or reflect those of the United States Government or any agency thereof."

Abstract

High Performance SOFCs with a Superior Stability for Reliable and Durable Power Systems

Next generation of fuel cells, electrolyzers, and batteries requires higher power, faster kinetics, and larger energy density, which necessitate the use of compositionally complex oxides to achieve multifunctionalities and activity. These compositionally complex oxides may change their phases and structures during an electrochemical process – a so-called "*electrochemically driven phase transformation*". The origin for such a phase change has remained obscure. More importantly, there is a need to develop high performance solid oxide fuel cells with an enhanced stability.

In this work, the $La_{0.6}Sr_{0.4}Co_{0.2}Fe_{0.8}O_3$ (LSCF) cathode surface is modified by infiltration of Pr_6O_{11} and the power density at 0.8V and 750 ^oC is improved by 21%. In addition, by replacing the traditional barrier layer $Gd_{0.2}Ce_{0.8}O_{1.9}$ with mixed conducting $Pr_{0.1}Gd_{0.1}Ce_{0.8}O_{1.9}$, the power density increases by 38%. The different mechanism of promotions was investigated by electrochemical impedance spectroscopy. The ohmic resistance is dramatically reduced by applying the PGCO interlayer, and the distribution of relaxation time was used to analyze the mechanism for which the polarization resistance was decreased attributing to the mixed conduction nature in PrO_x. An increase of power density at 0.8 V of 0.358 W/cm^2 (71%) is achieved with the implementation of both surface modification and buffer layer engineering.

An experimental study and a theoretical analysis were then carried out on phase evolution in praseodymium nickelates. Nickelate-based electrodes show up to 60× greater phase transformation during operation when compared to thermally annealed ones. Theoretical analysis suggests that the presence of a reduced oxygen partial pressure at the interface between the oxygen electrode and the electrolyte is the origin for the phase change in an oxygen electrode. Guided by the theory, an addition of the electronic conduction in the interface layer leads to the significant suppression of phase change, while improving cell performance and performance stability.

When an oxygen electrode is under polarization, the oxygen partial pressure at the interface between the oxygen electrode and the electrolyte is lower than that of incoming oxidant. Under a high polarization, the environment at the aforementioned interface may lead to phase transformation of the oxygen electrode. The local oxygen partial pressure is determined by the transport properties at the interfaces. An addition of the electronic conduction in the interface layer, for instance using (Pr,Gd)-doped ceria to replace Gd-doped ceria, results in improved cell performance and performance stability, while the phase transformation is significantly suppressed. This work provides a fundamental understanding of the origin for phase transformation in oxygen electrodes during operation and use this knowledge to develop a high-performance electrode that exhibits improved performance stability.

Contents

A. Executive Summary

Numerous projects have been funded for the research and development of solid oxide fuel cell (SOFC) power generation system since the start of DOE's Solid-State Energy Conversion Alliance in the fall of 1999 through the National Energy Technology Laboratory (NETL). The NETL SOFC Core Technology Programs aim at developing low-cost, highly efficient SOFC power generating systems that produce electrical power from natural gas or coal with intrinsic carbon capture capability. The technology is indeed on the brink of commercialization. A long-lasting challenge in SOFC R&D is to achieve high-performance and highly durable cells and subsequently understand the mechanism that underlies the strong correlation between activity and stability.

The polarization loss due to oxygen reduction at an oxygen electrode (cathode) in a solid oxide fuel cell, is a thermally activated process; therefore, as temperature is lowered, the loss becomes substantial. Highly active cathodes have been investigated extensively; equally important, if not more, is the stability of these electrodes, which still remains as a challenge area. The underlying question is: Why are active cathodes not stable; and stable cathodes not active – the so-called activity/stability conjugation? The proposed research emphasizes the evolution of electrode materials during operation, particularly cation kinetic demixing and investigate the role of interlayer chemistry on the cathode properties (activity and durability).

The work is driven by recognition of these experimental findings and theoretical analysis to rationalize the origin of demixing or phase transformation in the cathode by carrying out the following research activities: (1) to tune the electronic conduction in the cathode/electrolyte interlayer and investigate its role on the performance stability of the cathode by using conventional materials over the entire operational temperature range, and (2) to conduct theoretical analysis and in-situ diagnosis to elucidate the fundamental mechanism that determines the strong correlation between electrochemical activity and performance stability of the cathode. This project focuses on understanding the interlayer chemistry on the performance stability and cathode activity of laboratory-scale SOFCs. Various interlayers with a control over their electronic conductivity and porosity will be investigated. Theoretical analysis will be conducted to elucidate the role of interlayer on the evolution of the cathode electrochemistry and to guide the development of better electrodes.

B. Interlay Chemistry and Structure on Cathode Durability and Activity (Task 2)

B.1 Introduction

An SOFC enables the direct conversion of chemical energy stored in fuels into electricity without combustion, thus it can achieve a higher efficiency than the ideal Carnot engine in an environment-friendly manner[1]. The cathode which carries out the oxygen reduction reaction, contributes the significant amount to the total resistance, reducing the overall power density. Thus, the promotion of the cathode kinetics becomes a key to achieve an enhanced SOFC performance.

In recent years, $La_{1-x}Sr_xCo_{1-y}Fe_yO_3$ (LSCF) based perovskite material, which is a mixed oxygen ion and electron conductor, has been widely investigated as cathode in medium temperature SOFC applications[2]. Comparing to traditional $La_{1-x}Sr_xMnO_3$ (LSM) electrode for the high temperature SOFC applications, LSCF has a higher ionic conductivity[3], leading to expanded tripe phase boundary (TPB) in the cathode. However, extensive research works reveals that the Sr would segregate to the surface of LSCF electrode and result in the sluggish kinetics. The segregated SrO on the LSCF surface is not electrically conducive and reduces active sites for LSCF electrodes. The modification of the cathode surface by the solution infiltration could be a choice to revoke the oxygen reduction processes [4]. The precursor solution is infiltrated into the SOFC cathode and covers the surface of the cathode backbone. After calcining, the active particles are formed and bonded to the cathode surface therefore working as a catalyst for oxygen reduction. The infiltration of the stable electronically conductive LSM to the LSCF electrode increases the peak power density from 0.6 W/cm^2 to 0.8 W/cm^2.[5] Besides, some oxygen ion conductors such as doped ceria[6-7] and doped bismuth oxide[8] are also used for infiltration into LSCF electrode. The infiltrated LSCF with 14 vol% GDC can improve the electrode performance and durability by suppressing the Sr segregation.[9] PrOx has good electronic and ionic conductivies and it is often used in cathode modification to improve the electrode activity. By infiltration of PrOx into LSCF and STFC electrode, the peak power density increases from 0.28 W/cm^2 to 0.43 W/cm^2 for LSCF full cell and from 0.38 W/cm^2 to 1 W/cm^2 for STFC full cell at 650ºC.[10] The high oxygen ion diffusivity and surface exchange coefficient of PrOx lead to low electrode resistance (0.028 Ω cm^2) for PrOx infiltrated GDC electrode at 650ºC[11]. $Pr_2Ni_{0.5}Mn_{0.5}O_{4+\delta}$- and PrOx are impregnated into LSCF for proton conducting SOFCs to modify the cathode functionality and the peak power density reached

0.26 W/cm^2 at 650^{o}C, comparing to 0.16 W/cm^2 with a blank LSCF electrode[12]. Pr(III)/Pr(IV) redox couple in PrOx particle provides good oxygen reduction activity making it a candidate for infiltration to enhance cathode performance [13-14].

On the other hand, gadolinium doped ceria ($Gd_xCe_{1-x}O_{2-x}$, GDC) is widely used as the barrier layer to prevent interactions between cathode material and YSZ electrolyte at elevated temperatures owing to the low diffusion coefficient of Sr and La in ceria layer[15-16]. Denser GDC layer and oriented facet can further block the Sr diffusion and suppress the formation of $SrZrO_3$.[17] However, the ceria layer induces additional resistance in SOFCs. An additional GDC interlayer between LSM/YSZ cathode and YSZ electrolyte can significantly decrease cell performance[18]. SDC interlayer could contribute more than 60% ohmic resistance of the full cell with YSZ electrolyte[19]. The ceria layer can also be modified to improve interface stability and activity[20]. The Pr and Gd co-doped ceria, $Pr_{0.1}Gd_{0.1}Ce_{0.8}O_{1.9}$ (PGCO), which has higher electronic and similar total conductivity than GDC[21-23], is proved to suppress the phase evolution in $(Pr,Nd)_2NiO_4$ cathodes and achieve high and stable performance in our previous work[24-26].

In this work, a Pr/Gd co-doped ceria interlayer is applied between the $La_{0.6}Sr_{0.4}Co_{0.8}Fe_{0.2}O_3$ cathode backbone and YSZ electrolyte to replace the GDC interlayer. Pr containing precursor solution was infiltrated into the cathode to further investigate the feasibility of PGCO layer with the infiltrated electrode. The impedance results were analyzed with the distribution of relaxation time analysis to understand the performance promotion resulted from infiltrated PrOx and new ceria layer.

B.2 Experimental Method

B.2.1 Preparation of Powders and Electrodes

$Pr(NO_3)_3$, $Ce(NO_3)_3$ and $Gd(NO_3)_3$ (99.9%, Alfa Aesar, Haverhill, MA) were dissolved in de-ionized water and standardized by thermogravimetric analysis. Raw PGCO powders were synthesized by the glycine nitrate combustion process and calcined at 900 ^{o}C for 2 hours. Nano-sized PGCO and PrOx were synthesized by the semi-batch precipitation method[27] and dried at 100 ^{o}C for 24 hours. The powders were examined at room temperature by X-ray diffraction (XRD) using a Rigaku Miniflex 600 (Cu Kα) diffractometer equipped with D/teX detectors. The particle size was measured with Transmission Electron Microscopy (TEM, Hitachi 7600) at 80 kV. The calcined PGCO powders were mixed with the nano-PGCO at a weight ratio of 9:1. The V006 ink vehicle (Heraeus Inc, PA 19067) was then added to the powder mixture to form the PGCO ink. Terpinol was added into the ink to adjust its viscosity. The GDC ink was prepared by mixing GDC20 powder (100-400 nm), the nano-GDC (5-10 nm, GDC20-N, Fuelcellmaterials, Columbus, Ohio 43035), V006 ink vehicle and terpinol. The infiltration solution was prepared by dissolving stoichiometric citric acid in 2.5 g 1mmol/g $Pr(NO_3)_3$ to form a clear solution. Then 3 mL isopropanol was added to alter the surface tension of the solution. Nano-sized PrOx at 20 mol% was dispersed in the solution for infiltration. LSCF electrodes were infiltrated with 0.2 mL prepared solution, following by drying under vacuum. The infiltration was performed twice to obtain about 5 vol % Pr loading on the electrodes.

B.2.2 Fuel Cell Fabrication and Measurements

The bilayers consist of Ni-YSZ and YSZ electrolyte were prepared through a nonaqueous tape-casting and lamination process. The bilayer is of 1 inch in diameter and yields 40 vol% Ni and 60 vol% YSZ in the anode after reduction. The interlayer (PGCO or GDC) ink was screen-printed onto the bilayer and followed by sintering at 1200 ^{o}C for 2 hours. A 20 μm LSCF cathode was fabricated by screen printing and sintered at 1080 ^{o}C. Then the porous cathode was infiltrated and calcined at 900 ^{o}C for 30 minutes. The area of the active electrode was 2 cm^2. A gold grid was printed onto the cathode as the current collector.[28] The cross section of the cell was imaged with scanning electron microscope (SEM, Thermo scientific Scios 2) equipped with energy dispersive spectroscopy (EDS).

The cells were electrically connected to Pt wires in a 4-probe configuration and sealed on an alumina tube with glass paste. A quarter-inch alumina tube was used to provide air flow to the LSCF cathode. The chamber of the sealed tube was purged by nitrogen before NiO/YSZ anode was reduced by the hydrogen/nitrogen mixture for 1 hour. During electrochemical measurements, the Ni/YSZ anode was supplied with 3% humidified H_2 at a rate of 200 sccm and the LSCF cathode was fed with 400 sccm air. The electrochemical impedance spectrum (EIS) and current-voltage (i-V) curve were obtained by using a Biologic VMP3 multi-channel potentiostat (Bio-Logic USA, Knoxville, TN) equipped with external current boosters. The scan rate of i-V sweep is 5 mV/s and an alternating current of 10 mA/cm^2 amplitude was used in the impedance measurements from 0.1 Hz to 50 kHz.

B.3 Results and Discussion

B.3.1 Role of Interlayer Chemistry and Structure on the Performance of LSCF

(B3.1 is published in **International Journal of Hydrogen Energy, 47**, 1917-1924, 2022. https://doi.org/10.1016/j.ijhydene.2021.10.142)

Figure 1 shows the XRD pattern of PrOx and doped ceria. The PGCO prepared by combustion process are single-phased and share the same space group (Fm3m) with GDC. Therefore, doping Pr to GDC does not change the symmetry of lattices and Pr can fit into the lattice of ceria very well. PrOx has a monoclinic structure which is slightly distorted from cubic fluorite structure of ceria[29]. The PGCO particles synthesized from semi-batch reaction are observed from TEM (**Figure 3d**). The particle sizes are about 5 to 10 nm in diameter. To evaluate the reaction among the cathode, PGCO interlayer and electrolyte, the elemental analysis is performed in the PGCO interlayer and adjacent regions in the electrolyte and LSCF cathode (Figure S1). The cell is thermal annealed at 750C for 300 hours. No Pr, Ce, or Gd is observed in the YSZ electrolyte and LSCF cathode. Small amount of Zr (~0.71%) and Sr (~0.78%) is observed in the bulk of PGCO, which originates from the reaction between zirconia and ceria at sintering temperature. The Sr is migrated from cathode and reacted with zirconia while La, Co, or Fe isn't observed. PGCO has a good chemical feasibility with LSCF cathode and YSZ electrolyte.

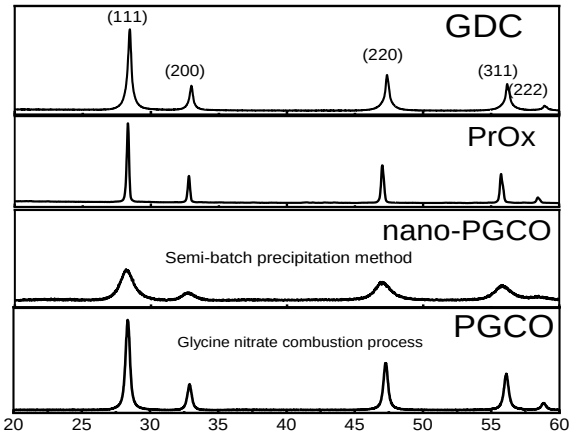

Figure 1. X-ray diffraction spectrum of GDC, PrO_x, PGCO powder.

The i-V and i-power density plots of cells are shown in **Figure 2**. Different treatment conditions of cells are listed in **Table I** and two cells are tested for each treatment to verify the reproducibility in performance. All cells are well-sealed with an open circuit voltage around 1.1 V. The power density of each cell at 0.8 V is listed in **Table I**. The performances were improved by 0.19 W/cm^2 and 0.11 W/cm^2 by applying PGCO interlayer and infiltrating PrOx into LSCF, respectively. By implementing both techniques, a further improvement of 0.358 W/cm^2 (71%) could be achieved. The total area specific resistances (ASRs) of the cells at different current density are calculated from the slope of the i-V curve, -dV/di, and shown in **Figure 2b**. The activation process leads to high resistance at low current densities (less than 0.2 A/cm^2).

The PrOx infiltrated LSCF cells with PGCO interlayer have a lower resistance at low current density which indicates the cathode processes are activated. As current densities range from 0.4 to 1.0 A/cm^2, the ASR values show a variation less than 0.1 Ω cm^2 demonstrating the linear behavior of the i-V curve in this region. The cells with PGCO have lower resistance in this region. Concentration polarization is evoked at high current (larger than 1.1 A/cm^2) where ASR starts to increase again. The total ASRs of different cells at 0.5 A/cm^2 are also compared in **Table I**. The decreased ASR after treatment leads to increased output power density.

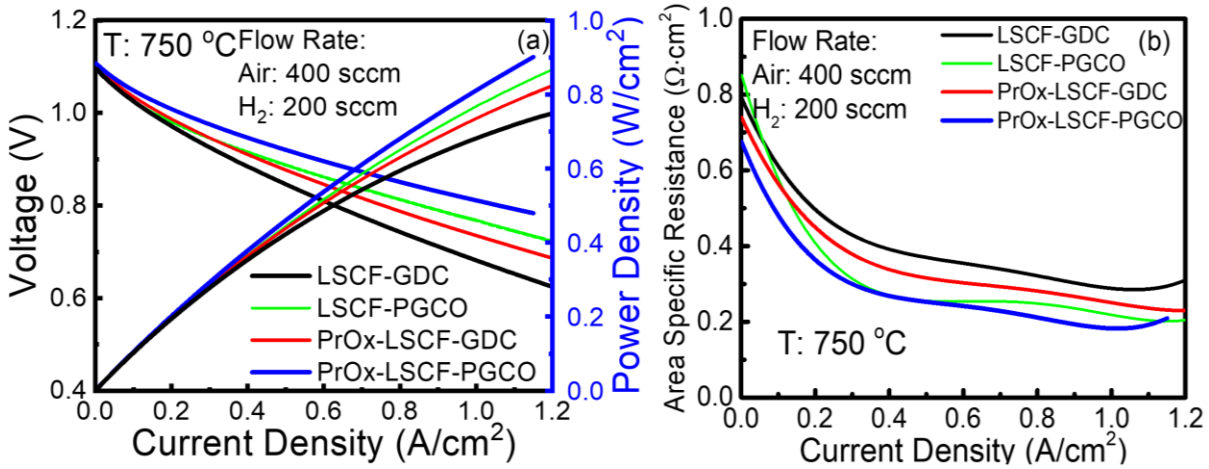

Figure 2. (a)The i-V and i-Power density curve of SOFCs with cathode after different treatment. (b) The total ASR of fuel cells generates from the i-V curve.

TABLE I. The Power Density and ASR of Different Cells			
Cell names	**Cell treatments**	**Power density at 0.8V (W/cm^2)**	**Total ASR @ 0.5A/cm^2 (Ω cm^2) from i-V**
LSCF-GDC	LSCF cathode on GDC interlayer	0.50	0.368
PrOx-LSCF-GDC	PrOx infiltrated LSCF cathode on GDC interlayer	0.61	0.315
LSCF-PGCO	LSCF cathode on PGCO interlayer	0.69	0.300
PrOx-LSCF-PGCO	PrOx infiltrated LSCF cathode on PGCO interlayer	0.85	0.253

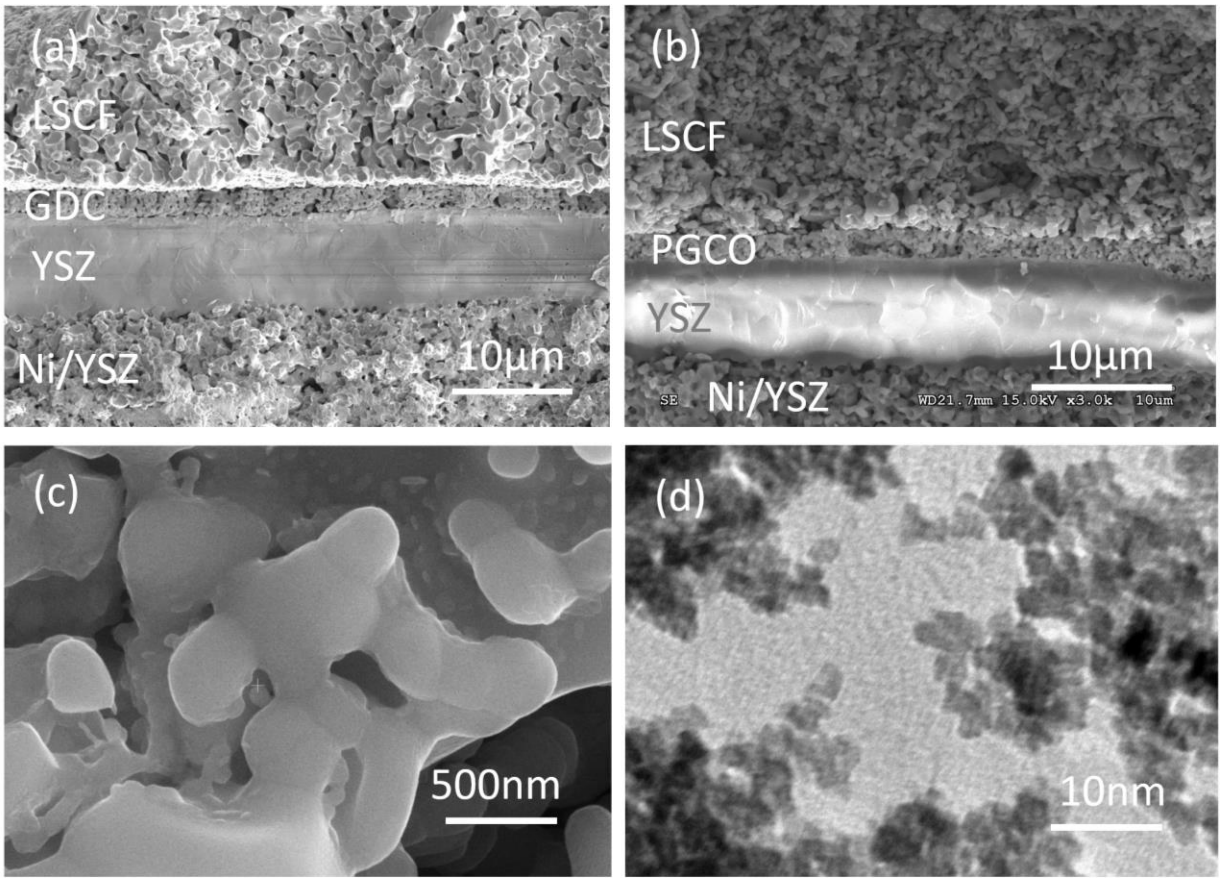

Figure 3. The SEM images of (a) cross-section of LSCF-GDC cell, (b) cross-section of LSCF-PGCO cells, (c) PrO_x infiltrated LSCF electrode and (d) the TEM image of PGCO nano particles.

To further understand the ASR reduction by introducing Pr species into the cells, the EISs are collected under open circuit and a direct current bias of 0.5 A/cm^2 and shown as Nyquist plots in **Figure 4**. The EISs are validated by Kramers-Kronig test with Lin-KK Tools.[30] The EIS at OCV shows the difference of ohmic resistance between GDC and PGCO layers. The highest total ASR of LSCF-PGCO cell at OCV also agree with the ASR plot at low current density region. As the current density increased up to 0.5 A/cm^2, ohmic resistances, which are contributed by the the electrical resistances of the cell components, don't change. The electrode resistance reduces and the resistance values from EIS at 0.5 A/cm^{2}are summarized in the **Table II**.

TABLE II. Ohmic and polarization resistance of individual cells at 0.5 A/cm^2		
Cell names	**Ohmic resistance (Ω cm^2)**	**Polarization resistance (Ω cm^2)**
LSCF-GDC	0.178	0.194
PrOx-LSCF-GDC	0.183	0.126
LSCF-PGCO	0.111	0.156
PrOx-LSCF-PGCO	0.124	0.119

The ohmic resistance, shown as the high-frequency intercept in the Nyquist plot, is reduced about 0.06 Ω cm^2 (about 33%) when the GDC is substituted by PGCO. The decreased ohmic resistance illustrates the decreased slope value in the linear region of i-V curve. The low-frequency intercept of Nyquist plot is the total ASR of the cell, which agrees with the result from DC measurement. The difference between the total and ohmic resistance is polarization resistance of the electrodes. The infiltration of the PrO_x into LSCF significantly reduces the polarization resistance, thereby indicating PrO_x promotes the cell performance by acting as catalyst in the cathode reactions. The PGCO interlayer also slightly decreases polarization resistance by about 15%, which implies that the novel ceria layer can potentially offer cathode activity. By doping praseodymium into ceria, the electronic conductivity of buffer layer is enhanced. By doping 3% Pr in GDC, the electronic conductivity can be improved by one order of magnitude[21]. The additional electronic conductivity provides triple phase boundary in the porous buffer layer for oxygen reduction reaction. **Figure 3** shows the SEM image of cross-section the fuel cells PrO-LSCF-GDC (a) and PrO-LSCF-PGCO (b). Two different interlayers are porous and of similar thickness, indicating the difference in ASR does not come from the geometry of ceria layer. **Figure 4** (c) shows the morphology of infiltrated LSCF electrode cross-section. Some infiltrated particles less than 100 nm can be seen on the surface of LSCF backbone. These infiltrated particles are active toward oxygen reduction reaction and reduces the polarization resistance.

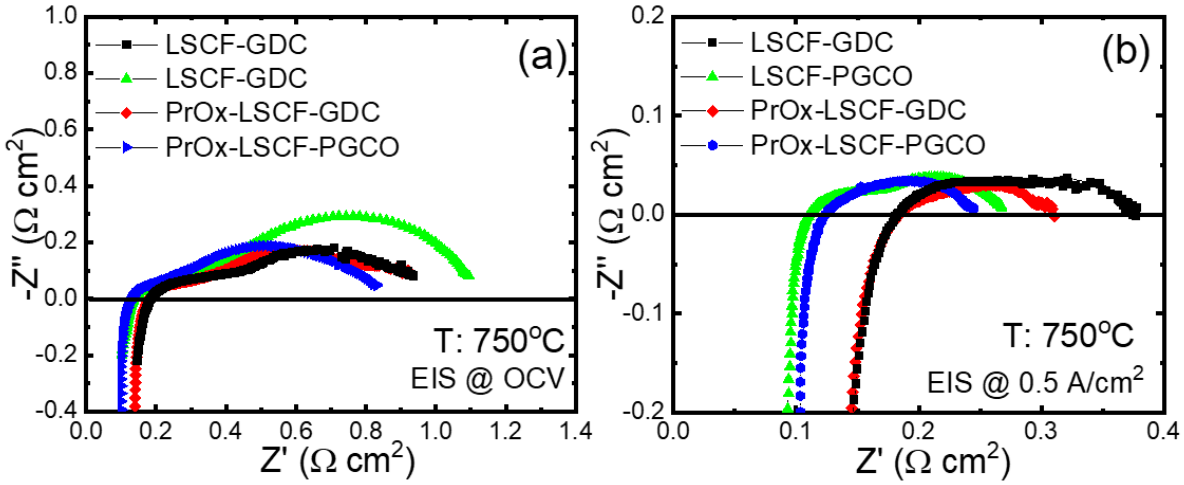

Figure 4. The initial EIS of different cells at (a) OCV and (b) an inject current density of 0.5 A/cm^2.

As previously shown, the electrochemical performance of SOFCs is commonly measured by i-V and electrochemical impedance spectroscopy. The i-V curve illustrates output power density at various current densities based on linear sweep voltammetry. EIS, which is based on alternating current, yields the impedance of a cell at various frequencies. According to the response of AC frequencies, there are two parts in a typical impedance spectrum: ohmic resistance and polarization impedance. The ohmic resistance is expected to be independent on the frequency, meaning it is in the high frequency intercept of the Z' axis. On another hand, the polarization impedance is a convoluted arch in a Nyquist plot and requires more analysis to be deconvoluted. The distribution of relaxation time (DRT) analysis converts the impedance in frequency domain into relaxation time domain[31-32]. The typical polarization impedance can be modeled by an integration of distribution function of relaxation time: $Z_{pol}(\omega) = \int_{-\infty}^{\infty} \frac{\gamma[\ln(\tau)]}{1+j\omega\tau}\, d[\ln(\tau)]$, where ω is the angular frequency (ω = 2πf), j is the imaginary unit, γ[ln(τ)] is the distribution function of relaxation time and τ is the relaxation time. DRT function separates dissipative processes with different relaxation times in the fuel cells into different peaks in relaxation time domain. The peak area represents the polarization resistance that is generated from the corresponding process.

EIS results are analyzed in the relaxation time domain by DRT to differentiate polarization resistances after subtracting the inductance contribution. DRT is performed with DRTtools and regularization parameter is set as 5×10^{-3}.[31] In **Figure 5**, five peaks, are shown in the DRT spectra and assigned to cathode and anode processes.[33] Each peak corresponds to at least one process which contributes to the polarization resistance. P_{1C} at about 0.1 to 1 Hz is low frequency cathode process, which is related to slower gas diffusion process in LSCF electrodes.[34] P_{1C} is higher in the PrOx infiltrated cells than respective cells without PrOx, which indicating PrOx particles offers more diffusion resistance. It may result from the dispersed highly active sites causes local concentration gradient. Fortunately, the diffusion effect is not dominating at low current densities. P_{1A} and P_{2C} at 1 Hz to 100 Hz are overlapped with each other, which are low frequency anode process and high frequency cathode process, respectively.

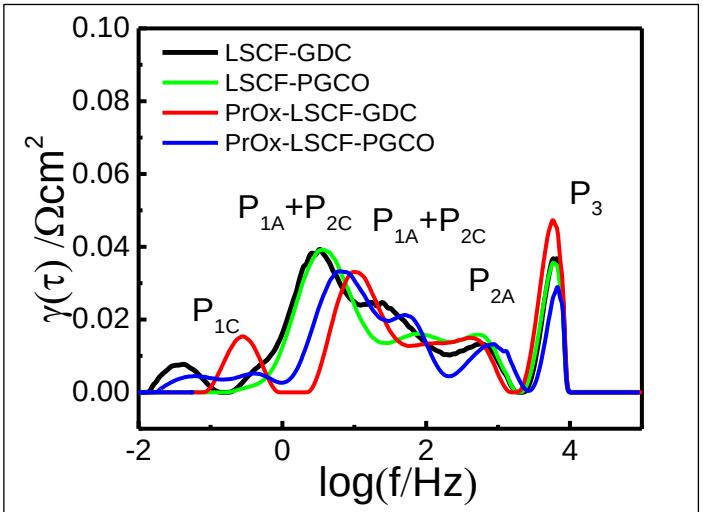

Figure 5. DRT spectrum of SOFCs at 0.5 A/cm^2.

P_{1A} is related to gas diffusion at the anode. P_{2C} is associated oxygen surface exchange kinetics on cathode surface and O^{2-} diffusion in the LSCF electrode,[35]. The associated peaks are clearly reduced in the infiltrated cell, indicating PrOx promotes the oxygen surface exchange and ion transport process, which contribute the major polarization resistance in the cell. Peaks P_{2A} at about 1kHz keep almost identical for all cells which is considered as a high frequency anode process. This peak is reported affected by p(H2O) in the anode gas and related to hydrogen oxidation kinetics in Ni/YSZ anode. Peak 3 is related to hydrogen oxidation kinetics which shows minimum

changes when the cathode is optimized.[35] P_3 at 10 kHz is assigned to high frequency charge transfer and ionic conduction process.[36] In general, PrOx can promote the oxygen surface exchange process which is of the highest resistance at operation condition to enhance the fuel cell performance. On the other and, the PGCO buffer layer does not lead to significant improvement in polarization resistance.

In addition, different PGCO thicknesses could be obtained by casting more layers or with a thicker screen. The PGCO cells with different thicknesses (**Figure 6** a, b, and c) are tested at 750°C and their electrochemical performance are shown in **Figure 6** d, e, and f. The cell with the thinnest PGCO layer has the best performance (0.68W/cm^2 at 0.8V) in the three cells. By an adding additional layer, the thickness of PGCO also increases up to 3.6 μm and the power density only dropped by 0.07W/cm^2 at 0.8V.

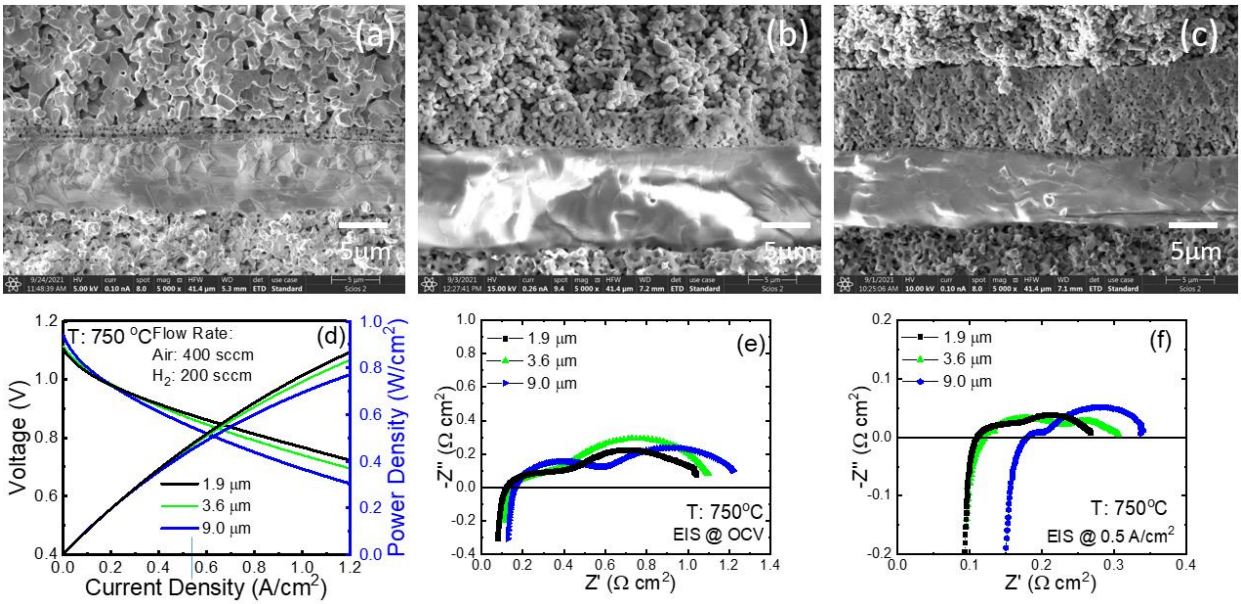

Figure 6 The SEM of the cross-section of the PGCO interlayer with a thickness of (a)1.9 μm, (b)3.6 μm and (c) 9.0 μm. The (d) IV (e) EIS@OCV and (f) EIS@0.5A/cm^2

A minor increase of ohmic resistance (about 0.008 Ω cm^2) is observed. By further increasing the thickness of the layer up to 9.0 μm, the ohmic resistance increases dramatically by another 0.06 Ω cm^{2}and result a significant drop in performance. Since the PGCO is not a good cathode material as LSCF[37], it generally plays a role as ionic conductor when it is significantly thick. Fabricate a dense and thin buffer layer always a right approach to its optimization for a high-performance fuel cell. The cell with thickest PGCO layer also has the highest polarization resistance at near OCV. While at the operation current, the polarization resistances are close to each other (0.157 for 1.9 μm, 0.187 for 3.6 μm, and 0.161 for 9.0 μm). By increasing the PGCO thickness up to 9 μm, the high frequency arch is reduced and shifts to a higher frequency, indicating an improved charge transfer process in the cathode.

All fuel cells were operating at a current density of 0.5 A/cm^2 for 400 hours. **Figure 7** shows their output voltage changed with time during the operation. The voltages dropped 3.5%, 2.8%, and

2.2% for the LSCF cell with GDC layer, infiltrated LSCF cell with GDC, and LSCF cell with PGCO barrier layer. This indicates that the cathode infiltration and interlayer optimization could enhance cell performance. Furthermore, the cell with PGCO interlayer and PrO_x infiltrated LSCF cathodes exhibits the better durability and power density than the other three cells, with only 0.7% voltage degradation after 400 hours. EISs of the cells are collected periodically to analyze the cell performance. The ohmic and polarization resistances are summarized in **Figure 8**. The ohmic degradation generally originates from the formation of insulative $SrZrO_3$ at the ceria/electrolyte boundary. By applying a PGCO interlayer, the ohmic degradation shows slightly decrease from 0.02 Ω (11.3%) to 0.01 Ω (9.0%). The Sr concentrations at ceria/YSZ interface are analyzed by EDS (**Figure 7** b) and listed in **Table III**.

TABLE III. Atom percent of Sr at ceria/YSZ interface after 400-hour operation	
Cell names	**Sr% at Ceria/YSZ interface**
LSCF-GDC	1.144
PrOx-LSCF-GDC	0.998
LSCF-PGCO	1.07
PrOx-LSCF-PGCO	1.01

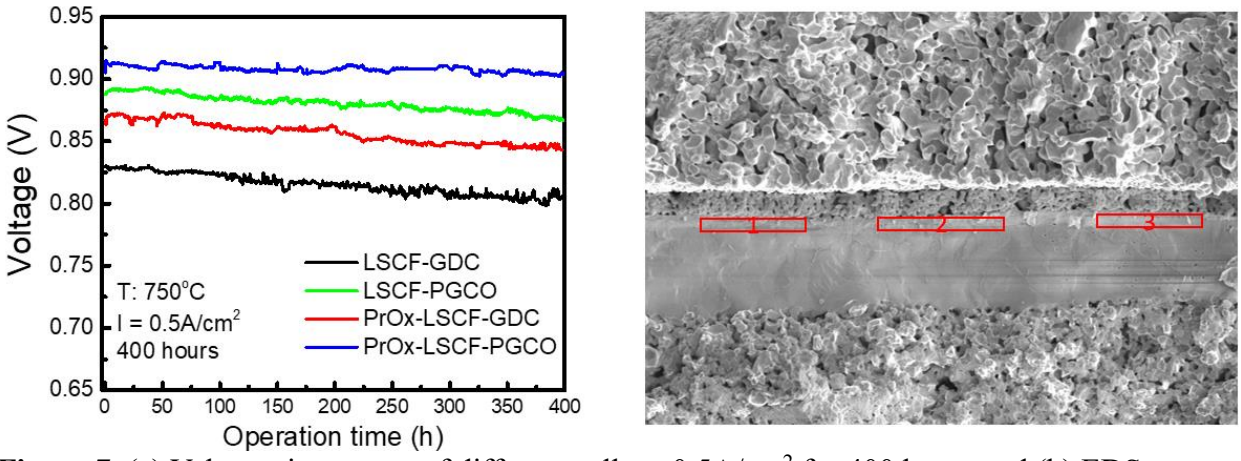

Figure 7. (a) Voltage-time curve of different cells at 0.5A/cm^2 for 400 hours and (b) EDS analysis at the ceria/electrolyte boundary.

The PGCO interlayer can block the direct reaction between LSCF and YSZ. But the migration of Sr to the YSZ surface is still observed and its concentration is about 1 atom% for all different cells after 400-hour operation. The slightly lower amount of deposited Sr with PGCO layer leads to a slightly lower ohmic degradation rate as GDC. PGCO could buffer the migration of Sr as a good substitute for GDC. The infiltration of PrO_x to LSCF backbone leads to a change of polarization degradation from 0.017 Ω to 0.014 Ω in 400 hours. Infiltration of active particles could suppress Sr segregation, which is a typical degradation mechanism of the bare LSCF electrode. However, the infiltrated cells suffer from nano PrO_x coarsening and loss of active surface area, [10] leading to the performance degradation of infiltrated LSCF electrodes.

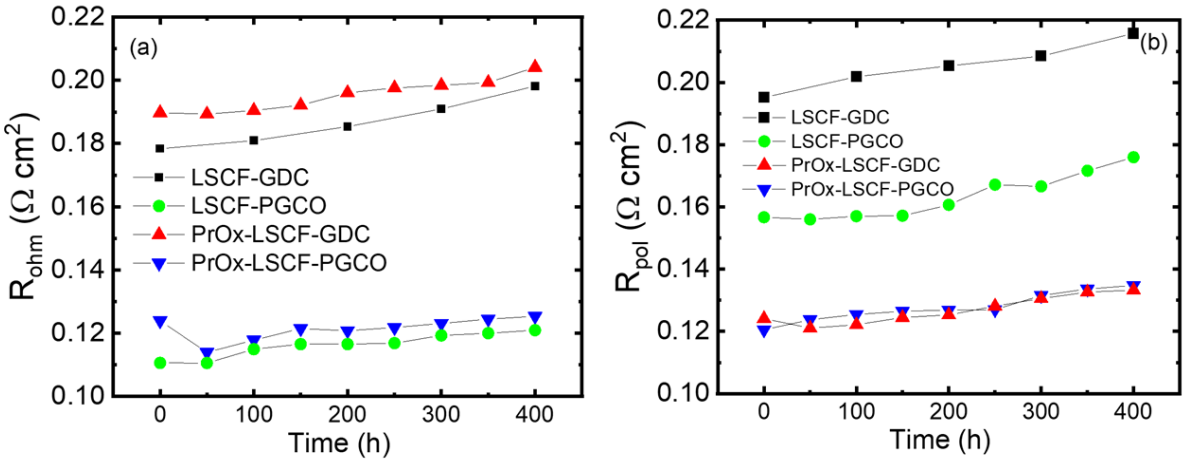

Figure 8. (a) Ohmic resistance and (b) polarization resistance of different cells at 0.5A/cm^2 during 400 hour-operation.

B.3.2 Role of Interlayer Chemistry and Structure on the Performance of Nickelates

(B3.2 is currently under revision for publication in ***The Proceedings of the National Academy of Sciences***)

The $(Pr_{1-x}Nd_x)_2NiO_4$ (PNNO) based oxygen electrode undergoes phase transformation into a Pr_6O_{11} (PrO_x) phase and a higher order $Pr_3Ni_2O_{7+\delta}$ phase at SOFC operation temperatures.[38] **Figure 9** shows the quantified phase transformation in PNNO electrodes that were treated with either thermally annealing or electrochemically operating in full cells at 750°C for 500 hours. The quantification method of phase transformation was reported previously.[28] Two sets of full cells show reproducible phase transformation, as shown in **Figure 9**. The percentage of phase transformation in thermally annealed electrodes is substantially lower than in operated electrodes.Clearly, accelerated phase transformation exists during an electrochemical operation. Since the phase transformation in operating nickelate electrodes has rarely been reported, this discrepancy is not yet addressed in the open literature. The parent compound without Nd substitution (x=0 in **Figure 9**), Pr_2NiO_4, is a known active oxygen electrode, which undergoes phase transformation during a thermally annealing process.[28, 38-41] The percentage of phase transformation in Pr_2NiO_4 was ~30% in an electrode annealed at 750°C for 500 hours. It, however, reached to nearly 100% when Pr_2NiO_4 was used as the cathode in a full cell at 750°C for 500

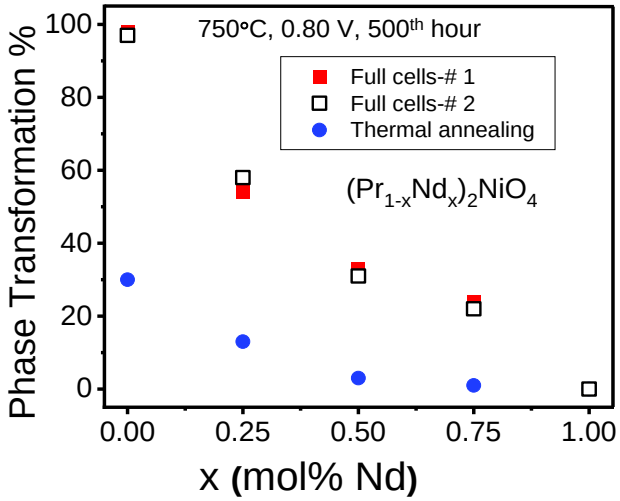

Figure 9. Phase evolution in thermally annealed electrodes (750°C, 500 hours) and electrochemically operated $(Pr_{1-x}Nd_x)_2NiO_4$ electrodes after 500 hours at 750°C and 0.80 V.

hours at 0.8 V. Two separated cells were examined and results were highly reproducible for all cathodes measured as a function of x in $(Pr_{1-x}Nd_x)_2NiO_4$. With an increase in x, the phase transformation is suppressed and it was fully suppressed in Nd_2NiO_4 (x=1)[39]

Figure 9 brings to a question as to what extent operating conditions influence the phase transformation in nickelate-based oxygen electrode. In order to establish the relationship between structural changes and cell operation, the phase transformation was studied as functions of operating temperatures and current densities. First, baselines were developed, including cathode before operation and thermal annealed electrodes. **Figure 10a** shows that operation of $(Pr_{0.50}Nd_{0.50})_2NiO_4$ (PNNO50-50) at 700 °C and 0.10 A/cm^2 for 300 hours does not lead to phase transformation, as shown by preserved parent phase. However, once the current density is raised to 0.50 A/cm^2 a clear phase evolution follows with the formation of PrO_x (+). Therefore, the phase transformation is indeed resulted from the electrochemical operation and must not be overlooked when quantifying phase evolution in an SOFC cathode. A systematic study at various temperatures and current densities was then carried out to understand"*electrochemically-driven phase transformation*".

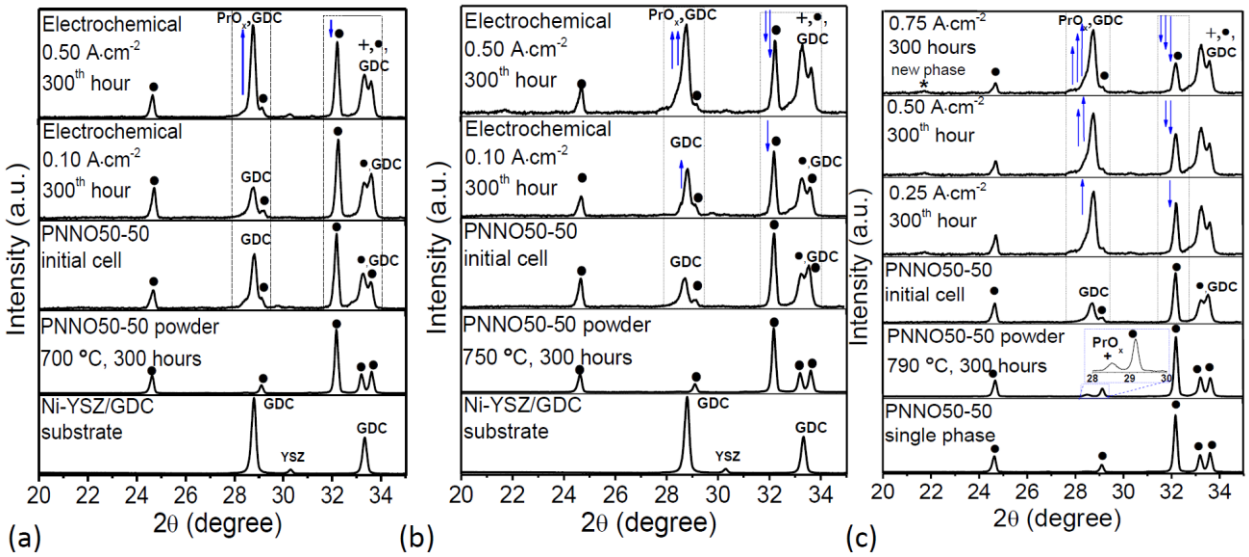

Figure 10. Phase evolution in PNNO electrodes operated under different current densities at (a) 700°C, (b) 750°C, and (c) 790°C. Standard XRD patterns for Ni-YSZ/GDC substrate and PNNO powder are shown in (a) and (b)**.**

As shown in **Figure 10b**, phase transformation was accelerated at 750°C at both 0.10 A/cm^2 and 0.50 A/cm^2. With an increase in current density the phase transformation increases. Similarly, the electrochemical operation in full cells at 790 °C leads to major phase transformation at 0.50 and 0.75 A/cm^2, as shown in **Figure 10c**. On the other hand, thermally annealed PNNO50-50 powders (between 700 – 790 °C) do not exhibit any significant phase transformation after 300 hours, consistent with the results shown in **Figure 9**. In fact, only ~1 mol. % of PrO_x is formed after 300 hours of annealing at 790 °C, **Figure 10c**.

Figure 11 summarizes quantified phase transformation in thermally annealed PNNO50-50 powders and electrodes, along with electrochemically operated cathodes. The plot was divided into two regions: (1) a region of thermally driven phase transformation, and (2) a region of

electrochemically driven phase changes. After 500 hours of annealing at 790 °C both powders and electrodes (YSZ/GDC/PNNO configuration) show only a few percent of phase transformation. A 1-2% larger phase transformation in electrode was detected due to previously discussed reaction with GDC interlayer.[39] However, it is clear that the electrochemical operation significantly accelerates phase transformation in nickelates. At 700 °C the PNNO50-50 electrodes operated at 0.50 A/cm^2 undergoes 10.6% phase transformation. With a further increase in temperature the phase transformation reached 15.5% at 750 °C and 0.50 A/cm^2. Even more evident results were obtained at 790 °C, where phase transformation was 60× larger than in thermal annealing studies at the same temperature. While the operation at a mild condition, 0.10 A/cm^2 and 700 °C, exhibited zero phase transformation, increasing temperature and operating time do show accelerated phase transformation, further indicating role of electrochemical operation on the phase evolution.

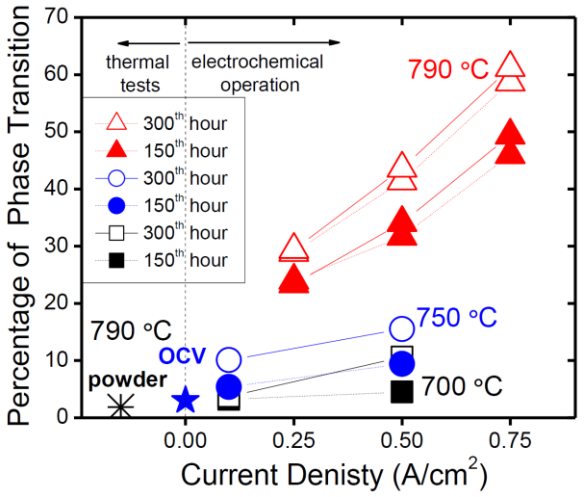

Figure 11. Quantified phase transformation in PNNO powders and electrodes. Powders and electrodes at OCV were thermally annealed at 790°C for 500h in air. Phase evolution in electrochemically operated electrodes is illustrated as function of current density at various temperatures and operating times.

As shown in the above discussion, one way to improve the local P_{O_2} at the cathode/electrolyte interface is to reduce the electronic resistance by introducing electronic conduction into the interlayer, for instance the presence of Pr[42]. **Figure 12a** illustrates a standard cell configuration with a conventional GDC20 interlayer. The first approach to design new interlayers involved a deposition of a thin Pr_6O_{11} film (~ 0.2 μm) on the top of GDC20 (named as PrO_x-GDC) with a Pr enriched zone at the boundary after sintering, as show in **Figure 12b**. The second approach is to tune the interlayer chemistry by using Pr/Gd co-doped ceria, $Pr_{0.10}Gd_{0.10}Ce_{0.80}O_{1.90\pm\delta}$ (PGCO), a bulk form rich with Pr, as shown in **Figure 12c**. **Table IV** summarizesthe materials and their functions in this study. These cell configurations were then used to study the role of the interlayer on phase transformation and performance stability of the cathodes. **Figure 12d** shows a scanning electron miscroscope image of a cell cross section, illustrating a respective thickness of each layer and a gold grid current collector, which allows for accurate phase evolution studies in cathodes.[38]

Table IV. A list of the materials, their chemical compositions, and functions.

Material	Chemical composition	Function
PNO	$Pr_2NiO_{4+\delta}$	Oxygen Electrode
PNNO	$(Pr_{1-x}Nd_x)_2NiO_{4+\delta}$	Oxygen Electrode

PNNO50-50	$(Pr_{0.5}Nd_{0.5})_2NiO_{4+\delta}$	Oxygen Electrode
GDC	$Gd_xCe_{1-x}O_{2-0.5x}$	Interlayer
GDC20	$Gd_{0.20}Ce_{0.80}O_{1.90}$	Interlayer
PGCO	$Pr_{0.10}Gd_{0.10}Ce_{0.80}O_{1.90}$	Interlayer

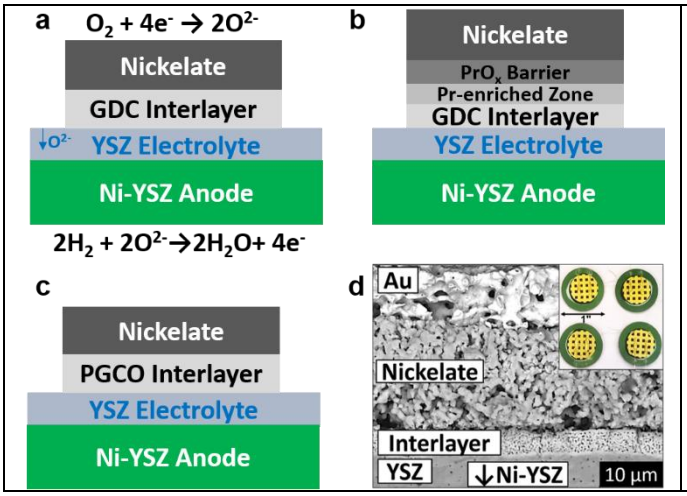

Figure 12. Schematics showing the overall electrochemical reaction in fuel cells and a nickelate electrode printed on (a) GDC20 (b) PrO_x-GDC, and (c) PGCO interlayers in full cell configuration. (d) Representative SEM image of a cell cross section showing respective thickness of each layer. A top view of Au grid (insert) is shown, which provides an exposure window for phase quantification studies. Nickelate represents for PNO or PNNO

Figure 13 (a) shows the current density as a function of time for PNO cathodes on various interlayers at 0.8 V. For each condition, two cells were measured. The results are reproducible and consistent among all cells. Remarkable performance stability was observed in cells with PGCO interlayer, with 0% degradation during 500-hour tests. Furthermore, the current density at 750 °C and 0.80 V was promoted by 27% (1.4 A/cm^2) with PGCO, in comparison with the use of a conventional GDC interlayer. With a conventional GDC interlayer, the decreases in fuel cell performance originate from the decomposition of Pr_2NiO_4 phase.[43] The cells with PrO_x-GDC interlayer exhibited better performance stability than with the conventional GDC. The decrease in r_e^c leads to a smaller oxygen chemcial potential gradient at the electrode/electrolyte interface, ($r_e^{c,PGCO} < r_e^{c,PrO_x-GDC} < r_e^{c,GDC}$). As a resault, the less reductive atomosphere with a mild $P_{O_2}^c$ value ($P_{O_2}^{cathode} > P_{O_2}^{c,PGCO} > P_{O_2}^{c,PrO_x-GDC} > P_{O_2}^{c,GDC}$) suppresses the phase transition in nickelate electrode so that the high performance is preserved.

Figure 13 (b) shows similar findings for the PNNO50-50 electrodes. Doping Nd into the Pr_2NiO_4 structure aims to improve the phase stability of the oxygen electrode.[44-45] A high performance with nearly zero-degradatin at 750 °C and 0.80 V was achieved with a PGCO interlayer. The consistent and reproducible measurements in multiple cells for each interlayer configuration and electrode composition indicate the reliability of our experimental approaches. What surprised us is that the performance of both PNO and PNNO5050 exhibits significantly improved performance stability over a 500-hour operation on PGCO layer. This is contradicted to an enduring assumption that the higher the activity, the less the performance stability. The observation of high-performance and highly stable cathode is, however, consistent with the theoretical analysis.

To further illustrate the relation between phase transformation and electrochemical operation with different interlayers, **Figure 14a** shows the phase evolution in PNO cathodes in operated full cells, as shown in **Figures 12 and 13a**. With GDC20, 45% of phase decomposition occurs, confirmed by evolution or PrOx (+) and a higher order $Pr_3Ni_2O_7$ phase (*). However, the cells with PGCO layer provide the most promising results. After 500 hours of electrochemical operation, the majority (87%) of the PNO phase (●) was preserved, which agrees with the better performance stability of the cell with PGCO than the one with GDC. In addition, PNNO cathode retained a completely stable structure with PGCO interlayer (initial ratio of peak intensities was preserved), as shown in **Figure 14b**. If a conventional GDC20 was used, despite the absence of formation of $Pr_3Ni_2O_7$ phase in PNNO electrodes, the evolution of PrOx peak ($2\theta \approx 29°$) is a clear indication of phase change. These results establish a correlation between phase transformation and electrochemical operation. A proper selection of the interlayer does play a significant role on stabilizing the parent phase. *In operando* XRD analysis in full cells at 750 °C and 0.80 V (**Figure 14c**) confirms the active phase at high current densities ($i \geq 1.0$ A/cm^2) is the prevalent high temperature nickelate phase. PrOx was not formed in PNNO50-50 electrode after 150 hours of electrochemical operation.

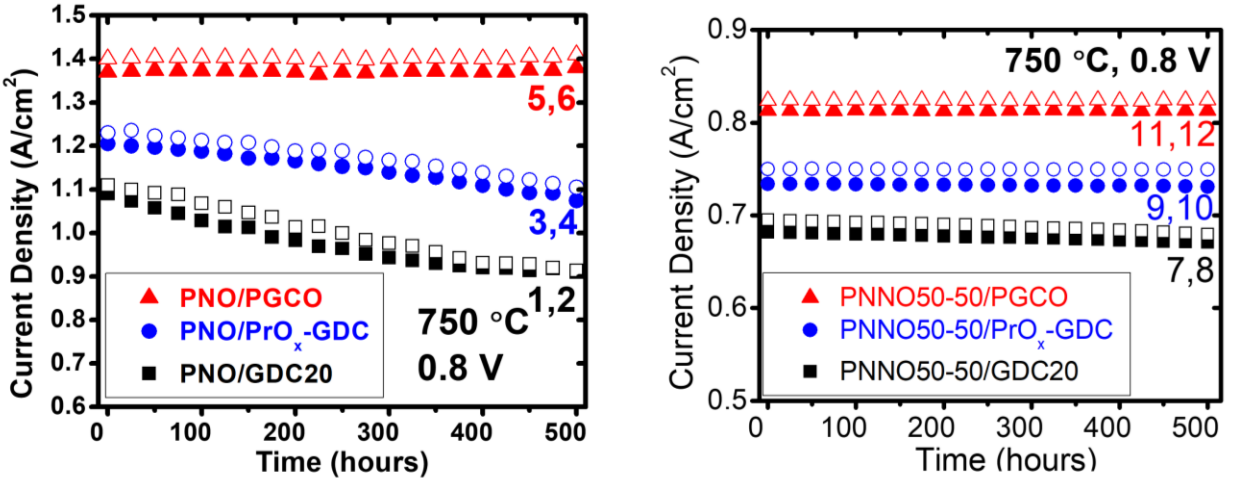

Figure 13. Electrochemial performance vs. time for (a) PNO and (b) PNNO full cells operated at 750 °C and 0.80 V. Two cells per each condition are shown. PGCO stands as $(Pr_{0.1}Gd_{0.1})Ce_{0.8}O_{1.9}$, as shown in **Figure 12c**. PrO_x-GDC corresponds to the configuration in **Figure 12b**.

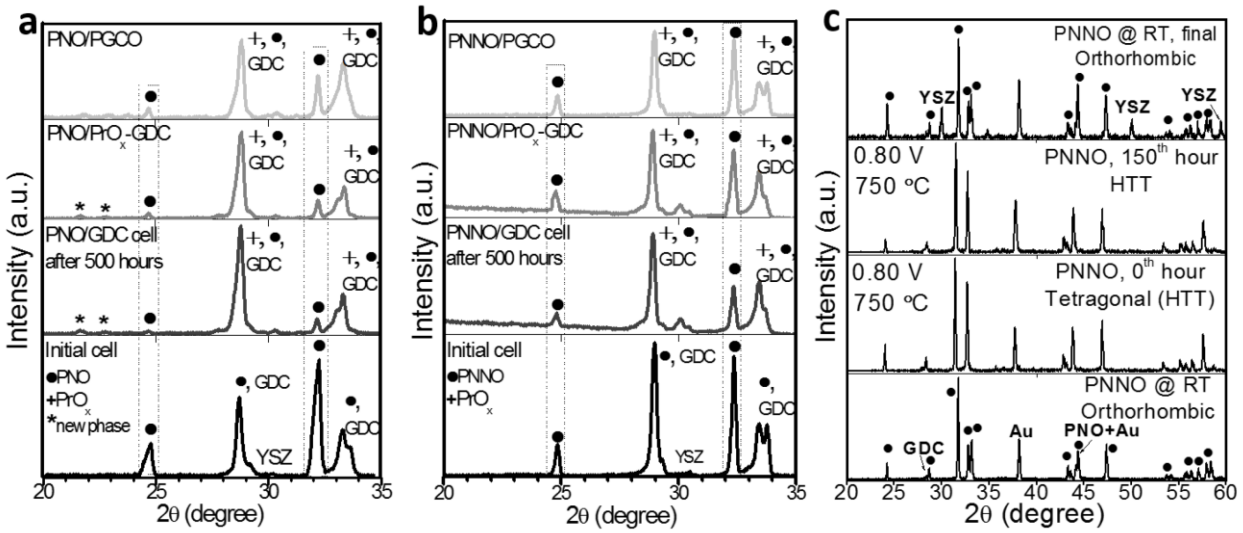

Figure 14 Phase evolution in (**a**) PNO and (**b**) PNNO50-50 electrodes operated in full cells at 750 °C and 0.80 V. The flux was normalized and peak positions were calibrated with multiple external (Ni-YSZ, single phase PNO and PrOx) and internal (Au) standards. An XRD pattern illustrated at the bottom shows initial cathode/GDC/YSZ/Ni-YSZ cell. Shown progressively from bottom to top are the final XRD patterns on cells with various interlayers. The cells with PGCO interlayer show preserved nickelate phase. (**c**) *In-situ* XRD patterns on operating PNNO electrode. Phase transformation from orthorhombic to tetragonal occurs at operating conditions. The parent nickelate phase in PNNO was fully preserved after operation.

B.4 Summary

Role of interlayer on LSCF performance. The infiltration of PrO_x to LSCF cathode and the addition of PGCO interlayer enhance the power density of the SOFC by 71 percent at 0.8 V and 750 ^oC. PrO_x are involved in oxygen reduction to improve cathode reaction kinetics, which can be supported from DRT analysis on the impedance spectrums. The ohmic resistance reduces by implementing the electronic conducting PGCO as the buffer layer between the cathode and electrolyte. The power density decreases by 0.6% when the cells are operated at $0.5A/cm^2$ for 400 hours. An electronic conductive doped ceria layer expands the TPB region and allows oxygen reduction reaction in ceria layer. Fabrication of a thinner, mixed conductive and dense buffer layer is the direction to reduce the ohmic loss during operation.

Role of interlayer on nickelate performance. When an oxygen electrode is under polarization, the oxygen partial pressure at the interface between the oxygen electrode and the electrolyte is lower than that of incoming oxidant. Under a high polarization, the environment at the aforementioned interface leads to phase transformation of the oxygen electrode. The local oxygen partial pressure is determined by the transport properties at the interfaces. An addition of the electronic conduction in the interface layer results in improved cell performance and performance stability, while the phase transformation is significantly suppressed.

C. Stability of the Cathodes in Reducing Conditions (Task 3)

The aim of this task is to summarize the effects of reducing conditions on our cathode materials Pr_2NiO_4 (PNO), $(Pr_{0.5}Nd_{0.5})_2NiO_4$ (PNNO), Nd_2NiO_4 (NNO), $(La_{0.8}Sr_{0.2})SrMnO_3$ (LSM20), and $(La_{0.6}Sr_{0.4})(Co_{0.2}Fe_{0.8})O_3$ (LSCF6428). Cathode powders were annealed at 750ºC for 25 to 500 hours in various atmospheres. The XRD analysis was carried out to study how the material has changed its structure during annealing. Results are shown in **Figures 15** to **18**. FullProf program was used to quantify the XRD data and give us information of the cell parameters.

Included in this report are the plots for all the tests completed. In nitrogen, the major change over time is the introduction of a second phase around the 150-hour mark. This change is present in the PNO, PNNO, and NNO materials (**Figures 15** and **16**). The two peaks right before the 35º mark started at the same height; however, at our current state, the left peak of the pair rises higher than the right. This is a sign that a new phase has formed. Using a phase information database, the space group of the new phase was identified to be I4/mmm, which is expected due to the higher symmetry than the initial phase, Bmab. A great amount of praseodymium oxide has been detected after 50-hour sintering.

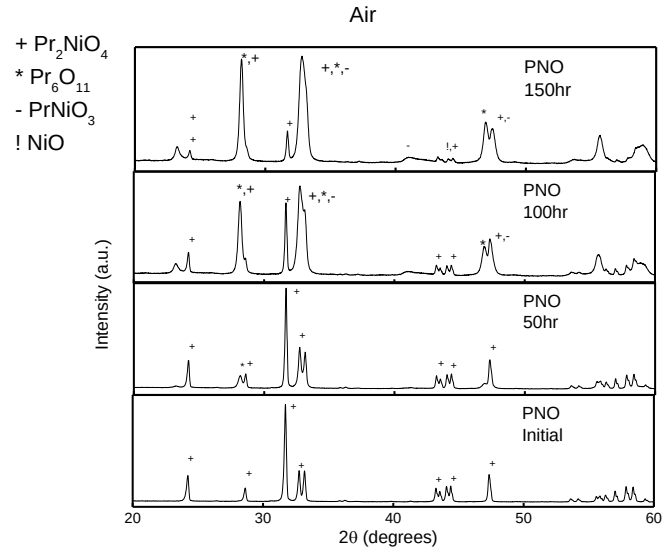

Figure 15. XRD pattens of PNO annealed at 750ºC for 50, 100, and 150 hours. The initial PNO diffraction pattern is incluced as a comparion.

Quantification was then performed. For example, Pr_2NiO_4, PNO, degrades to Pr_6O_{11}. Quantification is done by ratio between intensities between the original nickelate phases and the new PrOx phase. This plot shows the mole percentage of nickelate is transited into PrOx, NiO and higher order nickelates (**Figure 16)**. The calculation shows that, in nitrogen, the phase transition of PNO has been observed since 50th hour. The PNNO also shows phase transition for 200 hours, but the rate is much slower. No obvious phase degradation was observed in NNO for 200 hours. The phase transition rate of PNO in N_2 is about 4% in 200 hours and the rate of PNNO is about 1% in 200 hours. This also shows how high the rate of degradation in the presence of air is in comparison to that of nitrogen.

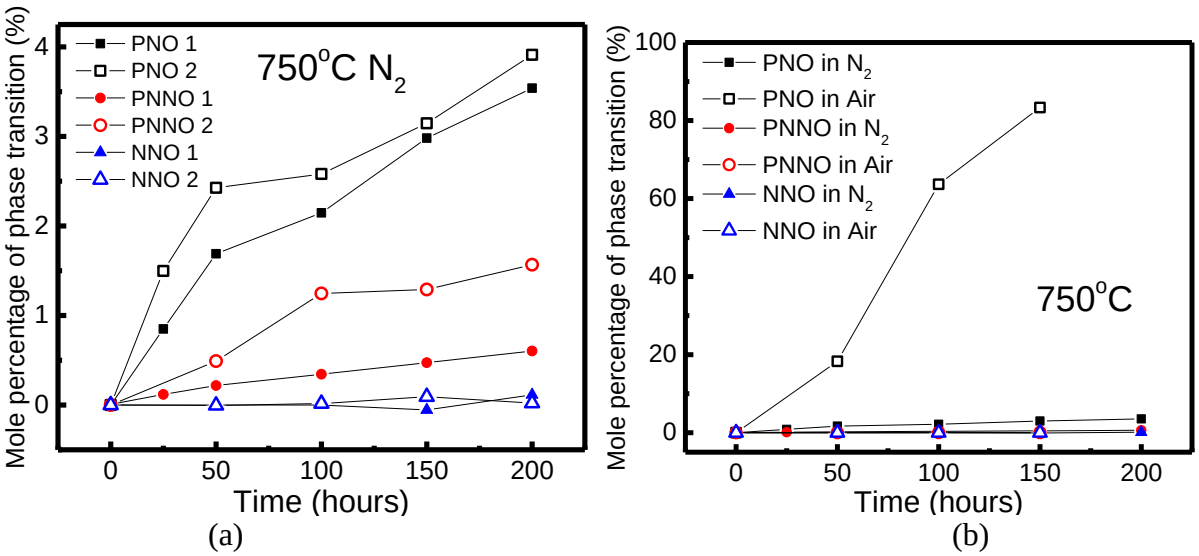

Figure 16. (a) XRD pattens of PNO, PNNO, and NNO, annealed in N_2 at 750°C. Two specimens were used for each composition. (b) A comparison of PNO, PNNO, and NNO annealed in air and N_2 at 750°C.

The cell parameters for each material were calculated in the presence of N_2. For the first phase, the a-values slightly decrease, the b-values increasing, and the c-values decreasing. Few data points were collected of the second phase of these powders, but with the points obtained, it appears that NNO has the most consistent parameters in the second phase. In the presence of nitrogen, NNO was the least affected in terms of degradation, proving to be the most stable. The study of the material degradation in the presence of air is still ongoing, but it appears that PNO will continue to undergo rapid degradation in a relatively small amount of time. About 85% of original PNO phases were decomposed in 150 hours. Comparing to the 3% degradation under nitrogen, PNO is more stable while annealing under nitrogen.

For LSCF6428, **Figure 17** shows that the structure of LSCF6428 remain the same during the annealing processes in both air and N_2. Annealing in N_2, however, does result in a shift of diffraction peaks to a lower angle, suggesting an increase in cell parameters. The chemical expansion of LSCF and (La,Sr)$FeO_{3+\delta}$ is well documented. **Figure 18** shows the LSM20 annealed in air and N_2. The structure and diffraction peaks remain unchanged during annealing.

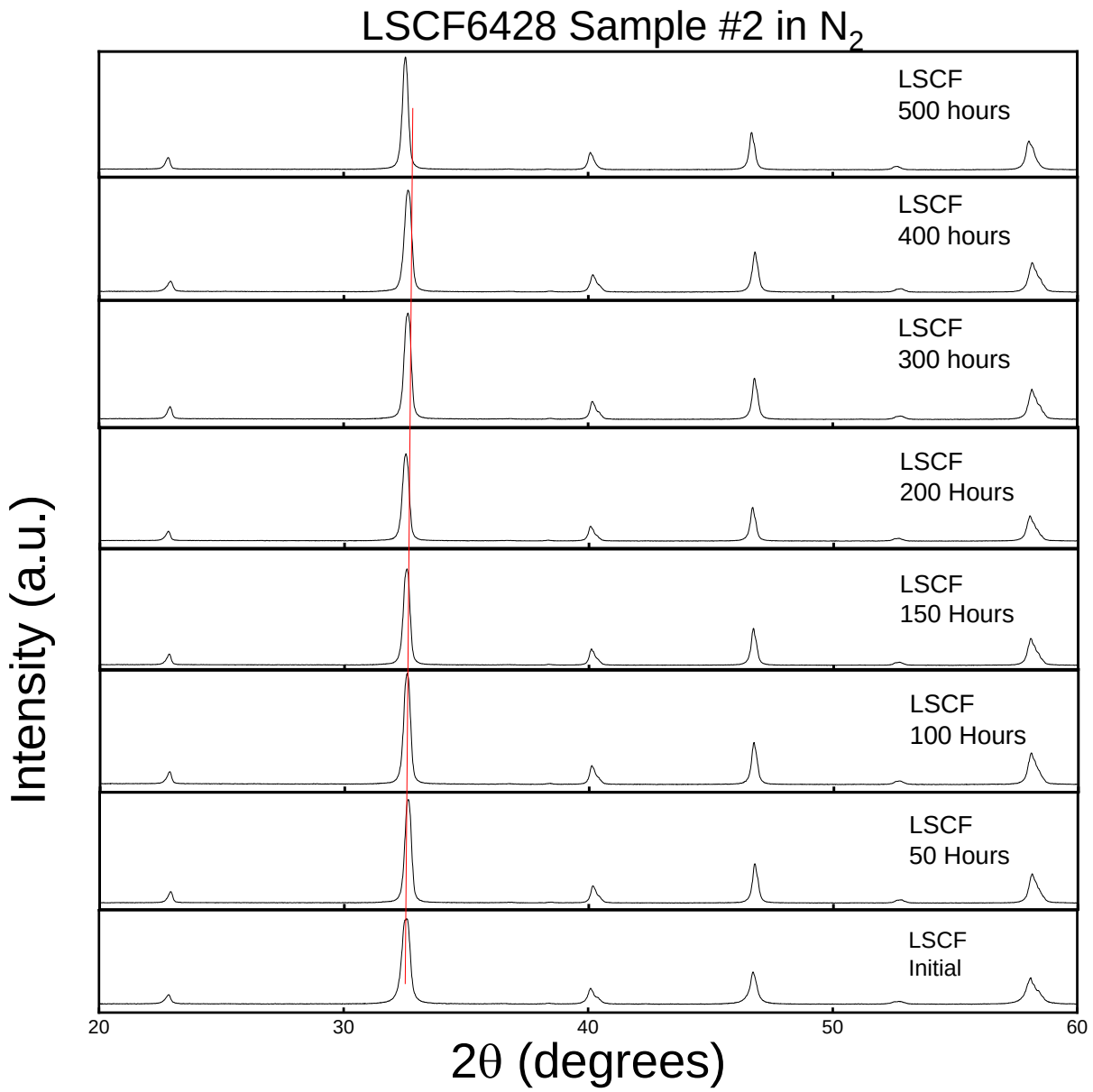

Figure 17. LSCF6428 annealed in nitrogen as a function of time. The diffraction pattern of initial LSCF6428 is included as a baseline comparison. A shift of diffraction peaks to lower angles is observed with an increase in annealing time, suggesting an increase in lattice parameter.

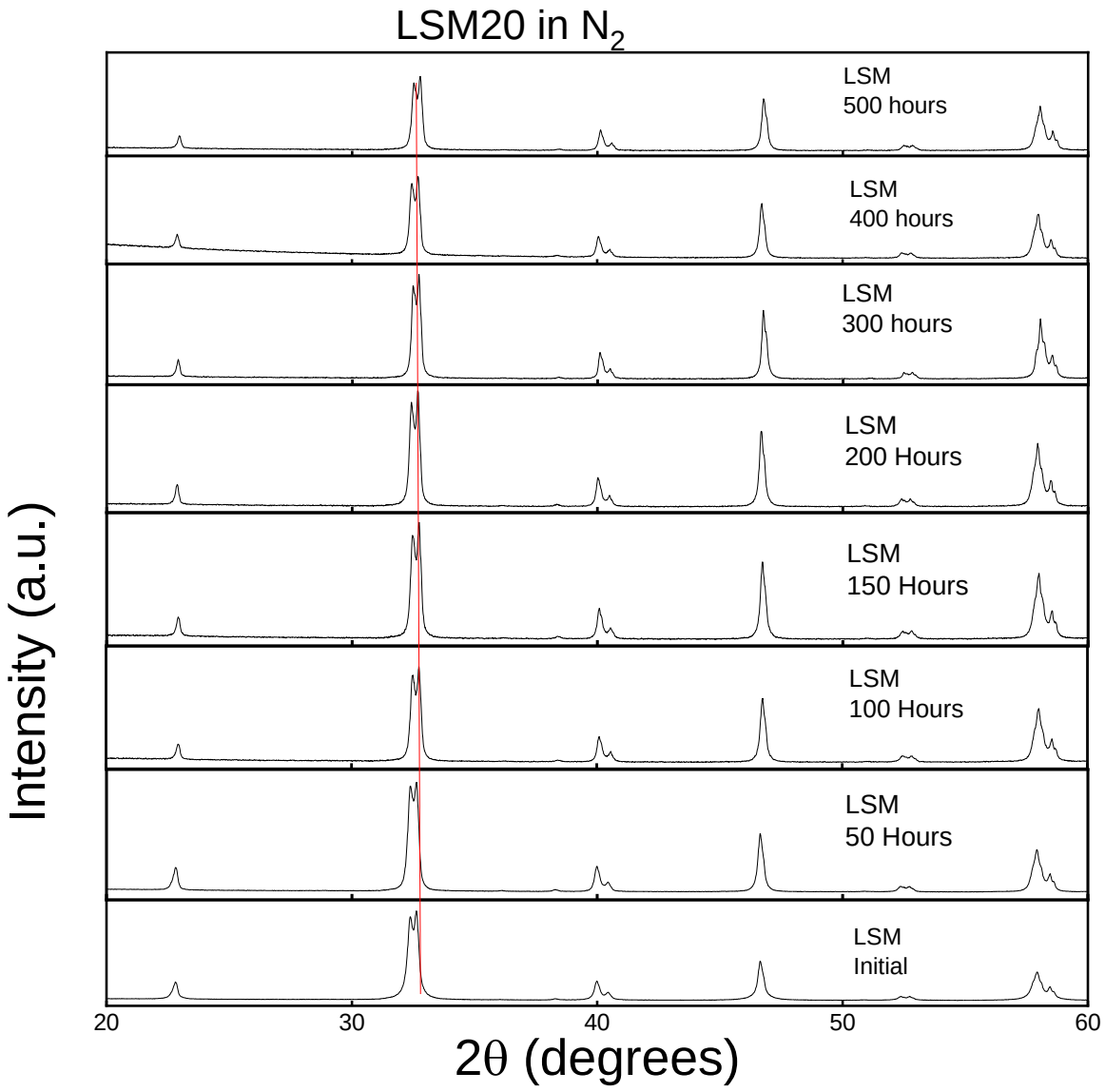

Figure 18. LSM20 annealed in nitrogen as a function of time. The diffraction pattern of initial LSM20 is included as a baseline comparison. The structure remains the same as a fucntion of annealing time.

D. Theoretical Analysis (Task 4)

An electrochemical cell is a typical non-equilibrium system, which involves the coupling of electrical currents and flux of different ions and neutral species.[46-48] Thus, non-equilibrium thermodynamics is of great necessity to study the phenomenon in solid-state electrochemical system.[49] Eventually, most continuum modeling works are based on the natural concept of local equilibrium so that the state variable can be defined locally. The concept of non-equilibrium is

widely used in fuel cells[50-51], batteries [52-54] and electrolyzers.[46, 55-56] Most research works are focusing on the kinetics or stability of the electrodes. William et. al. studied the origin and physics of the activation overpotential based on non-equilibrium thermodynamic understanding of electronic defects in $Gd_{0.2}Ce_{0.8}O_{1.9}$ (GDC) via two phase boundary (2PB) path or three phase boundary path (3PB) for a Ni/GDC fuel electrode.[57] The capacity of lithium-air battery is associated with the formation of Li_2O_2 species on the active site of the porous oxygen electrode, and the formation of Li_2O_2 was analyzed by the coupling of oxygen, electron and ion transport.[58] The cracking phenomenon in polycrystalline lithium cathode was studied from a non-equilibrium thermodynamic perspective based on a chemo-mechanical coupled model[59].

Non-zero electronic current is a key implication of local equilibrium assumption, which indicates that even in a predominantly ionic conductor, the electronic current cannot be entirely neglected. That is, even though the magnitude of the electronic current in a typical ionic conductor is often negligible in comparison to the ionic current, it still cannot be set identically to zero. This is because the electronic transport, however small, plays a decisive role in the establishment of the above equilibrium and thus in the establishment of the local chemical potential of oxygen, $\mu_{O_2}(\vec{r})$, which in turn dictates the very stability of the membrane.

In terms of electronic current density, I_e, *through* the electrolyte and ionic current density, I_i, through the electrolyte, the chemical potential of oxygen on a per molecule basis, μ_{O_2}, in the electrolyte just inside cathode ($\mu^c_{O_2}$), as shown in **Figure 19**, is given by[51]:

$$\mu^c_{O_2} = \mu^{cathode}_{O_2} + 4e(r^c_i I_i - r^c_e I_e) \quad [1]$$

where $\mu^{cathode}_{O_2}$ is the μ_{O_2} in the cathode gas, r^c_i is the ionic interfacial ASR at the cathode/electrolyte interface, and r^c_e is the electronic interfacial ASR at the cathode/electrolyte interface. The oxygen ion flux through the electrolyte occurs from the cathode to the anode. Thus, ionic current density $I_i < 0$.

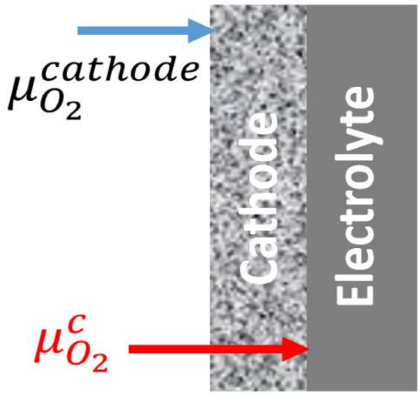

Figure 19. A schematic of locations for $\mu^{cathode}_{O_2}$ and μ_{O_2} in an SOFC.

When a cell is operating normally, cathode is at a higher electric potential, φ, than the anode: where $\varphi = -\tilde{\mu}_e/e$ and $\tilde{\mu}_e = \mu_e - e\Phi$ is the electrochemical potential of electrons, μ_e is the chemical potential of electrons, e is electronic charge, and Φ is electrostatic potential. Thus, electron flux *through* the electrolyte, however small, occurs from anode to cathode, and the electronic current density $I_e > 0$. That is, I_i and I_e are of opposite signs. Hence, when a cell is operating properly (normally), one can obtain:

$$\mu_{O_2}^{c} = \mu_{O_2}^{cathode} + 4e(r_i^c I_i - r_e^c I_e) = \mu_{O_2}^{cathode} - 4e(r_i^c|I_i| + r_e^c|I_e|) < \mu_{O_2}^{cathode} \quad [2]$$

Assuming the ideal gas law for oxygen, one obtains $\mu_{O_2}^{cathode} = \mu_{O_2}^{o} + k_B T ln(P_{O_2}^{cathode})$, where $\mu_{O_2}^{o}$ is standard state gas phase oxygen chemical potential and $P_{O_2}^{cathode}$ is the oxygen partial pressure at the cathode (gas phase). Eq. [31] gives:

$$P_{O_2}^{c} \approx P_{O_2}^{cathode} \exp\left[-\frac{4e(r_i^c|I_i| + r_e^c|I_e|)}{k_B T}\right] \quad [3]$$

which shows that $P_{O_2}^{c} < P_{O_2}^{cathode}$. In order to estimate the possible magnitude of $P_{O_2}^{c}$, numerical estimates are presented in what follows for assumed values of parameters. The magnitude of the pressure difference is dependent upon the $(r_i^c|I_i| + r_e^c|I_e|)$. Let the operating temperature be 800 °C (1073 K). Also, let us assume that $(r_i^c|I_i| + r_e^c|I_e|)$ = 0.2 V, suggesting the cell potential gradient at the cathode is 0.2 V. Then with air as the oxidant ($P_{O_2}^{cathode}$ = 0.21 atm), the estimated $P_{O_2}^{c} \approx 3.7 \times 10^{-5}$ atm, a reducing environment that can indeed change the stability of a cathode. The local oxygen partial pressure (the level of reducing condition) depends on both $r_i^c|I_i|$ and $r_e^c|I_e|$. The most reducing location is at the immediate cathode/electrolyte interface. **Table VI** lists the magnitude of $P_{O_2}^{c}$ as a function of cathodic potential gradient. The greater $P_{O_2}^{c}$, the more stable the cathode is during operation. If the cathode potential gradient is 0.4 V, the local $P_{O_2}^{c}$ is as low as 6.5×10^{-9} at which both LSCF and nickelates will go through severe phase change.

Moreover, as shown in Eq. [3], the chemical potential, thus oxygen partial pressure, in the interlayer is exponentially dependent on $r_i^c|I_i| + r_e^c|I_e|$, in which r_i^c and r_e^c can be tuned. As a result, to reduce the electronic resistance by introducing an electronic conductor into the interlayer, for instance the presence of Pr.

Table VI. Oxygen partial pressure ($P_{O_2}^{c}$) at the cathode/electrolyte interface as a function of the cathode potential gradient.

Potential gradient	0.05 V	0.1 V	0.2 V	0.3 V	0.4 V
$P_{O_2}^{c}$ (atm)	0.024	0.0029	3.7×10^{-5}	4.9×10^{-7}	6.5×10^{-9}

E. Cost Status

COST PLAN/STATUS In $

	FY2019: 10/01/18-09/30/19				FY2020				FY21		Total
	Q1	Q2	Q3	Q4	Q1	Q2	Q3	Q4	Q1	Q2	
Forecasted											
Federal	50000	50000	60000	60000	50000	60000	60000	60000	49999	0	499,999
Non- federal	12500	12500	15000	15000	12500	15000	15000	15000	12500	0	125,000
Total	62,500	62,500	75,000	75,000	62,500	75,000	75,000	75,000	62,500	0	625,000
											0
Actual											0
Federal	10000	15000	20000	20000	80000	80000	80000	80000	80000	35000	500,000
Non- federal	2500	3750	5000	5000	20000	20000	20000	20000	20000	8750	125,000
Total	12,500	18,750	25,000	25,000	100,000	100,000	100,000	100,000	100,000	43,750	625,000
											0
Variance											0
Federal	-40000	-35000	-40000	-40000	30000	20000	20000	20000	30000	35000	0
Non- federal	-10000	-8750	-10000	-10000	7500	5000	5000	5000	7500	8750	0
Total quarterly	-50,000	-43,750	-50,000	-50,000	37,500	25,000	25,000	25,000	37,500	43,750	0
Cumulative Variance	-50,000	-93,750	-143,750	-193,750	-156,250	-131,250	-106,250	-81,250	-43,750	43,750	0

F. Milestone Charts

				FY19				FY20				FY21			
	Start Date	End Date	Cost	Q1	Q2	Q3	Q4	Q1	Q2	Q3	Q4	Q1	Q2	Q3	Q4
Task 1. Project Management, Planning and Reporting	10/1/2018	9/30/2021	$124,999												
Subtask 1.1 - Project Management and Planning	10/1/2018	9/30/2021													
Subtask 1.2 - Briefings and Reports	10/1/2018	9/30/2021													
Task 2.0 - Interlayer chemistry and structure			$300,000												
Subtask 2.1 - Baseline Measurements	10/1/2018	9/30/2019													
Subtask 2.2 - Rol of interlayer chemistry (dense)	10/1/2019	9/30/2021													
Subtask 2.3 - Role of interlayer chemistry (porous)	1/1/2019	12/30/2020													
Milestones															
Milestone 1: Promoting performance in cathodes	10/1/2019	12/30/2021										❶ 12/30/20			
Milestone 2: Superior stability at a high current density	10/2/2019														❷ 9/30/21
Task 3.0 - Stability of the cathodes in reducing conditions	10/1/2018	6/30/2020	$100,000												
Milestone 3: Characterization of cathode stability vs.	10/1/2018	9/30/2020									❸ 9/30/20				
Task 4.0 Theoretical analysis	10/1/2018	6/30/2021	$100,000												
Milestone 4: Validation of theroretical analysis	10/1/2018													❹ 3/30/21	

G. Personnel

Dr. Xiao-Dong Zhou is a Professor in the Department of Chemical Engineering at University of Louisiana at Lafayette. Prior to that, he was a Professor at University of South Carolina (USC) and a Senior Research Scientist at the Pacific Northwest National Laboratory from 2005-2010. He obtained his Ph.D. in Ceramic Engineering from University of Missouri Rolla. Dr. Zhou received *J. B. Wagner Jr. Young Investigator Award* in 2007 from the Electrochemistry Society (ECS) - High Temperature Materials Division and DOD DARPA's Young Faculty Award in 2011. He currently serves as the Chair for the division. Dr. Zhou's research interest focuses on synthesis, characterization and theoretical understanding of materials for SOFCs. Since 2001, his career has been highlighted by 80 peer-reviewed articles that are related to the proposed research. In addition, he has published 8 invited book chapters, contributed to over 100 presentations; and received 6 US patents/disclosures. He is an associate editor of the Journal of the American Ceramic Society.

Mr. Yudong Wang (Graduate Student): Yudong Wang is a Ph.D. candidate in Prof. Zhou's group. He obtained his B.S. degree in chemistry from University of Science and Technology of China. Currently, he is working on structural and electrochemical analysis of Ruddlesden-Popper type MIEC cathode materials to understand the material stability and system performance under operating conditions.

Mr. Josh Wilson is a graduate student working in the PI's group. He received B.S. degree from the Chemical Engineering Department at UL Lafayette. Mr. Wilson's research will focus on the innovative SOFC development.

Undergraduate: The PI will leverage the Undergraduate Research Fellowships and NSF Research Experience for Undergraduates at UL Lafayette to build a diverse group that includes women and members of underrepresented minority groups. The undergraduates from the PI's group will be encouraged to enroll in the Honors College and to continue further graduate research by applying for graduate fellowships.

H. References

1. Minh, N. Q., Ceramic Fuel Cells. *Journal of the American Ceramic Society* **1993,** *76* (3), 563-588.
2. Jiang, S. P., Development of lanthanum strontium cobalt ferrite perovskite electrodes of solid oxide fuel cells – A review. *International Journal of Hydrogen Energy* **2019,** *44* (14), 7448-7493.
3. Teraoka, Y.; Nobunaga, T.; Okamoto, K.; Miura, N.; Yamazoe, N., Influence of constituent metal cations in substituted LaCoO3 on mixed conductivity and oxygen permeability. *Solid State Ionics* **1991,** *48* (3), 207-212.
4. Ding, D.; Li, X.; Lai, S. Y.; Gerdes, K.; Liu, M., Enhancing SOFC cathode performance by surface modification through infiltration. *Energy & Environmental Science* **2014,** *7* (2), 552-575.
5. Liu, Z.; Liu, M.; Yang, L.; Liu, M., LSM-infiltrated LSCF cathodes for solid oxide fuel cells. *Journal of Energy Chemistry* **2013,** *22* (4), 555-559.
6. Nie, L.; Liu, M.; Zhang, Y.; Liu, M., La0.6Sr0.4Co0.2Fe0.8O3−δ cathodes infiltrated with samarium-doped cerium oxide for solid oxide fuel cells. *Journal of Power Sources* **2010,** *195* (15), 4704-4708.
7. Burye, T. E.; Nicholas, J. D., Nano-ceria pre-infiltration improves La0.6Sr0.4Co0.8Fe0.2O3−x infiltrated Solid Oxide Fuel Cell cathode performance. *Journal of Power Sources* **2015,** *300*, 402-412.
8. Li, G.; He, B.; Ling, Y.; Xu, J.; Zhao, L., Highly active YSB infiltrated LSCF cathode for proton conducting solid oxide fuel cells. *International Journal of Hydrogen Energy* **2015,** *40* (39), 13576-13582.
9. Zhang, Y.; Nicholas, J. D., Evidence that Surface-Segregated Sr Phases Can Be Removed in LSCF via Ceria Pre-Infiltration, Are Less Apt to Form in SSC. *Journal of The Electrochemical Society* **2021,** *168* (2), 024522.
10. Lu, M. Y.; Scipioni, R.; Park, B.-K.; Yang, T.; Chart, Y. A.; Barnett, S. A., Mechanisms of PrOx performance enhancement of oxygen electrodes for low and intermediate temperature solid oxide fuel cells. *Materials Today Energy* **2019,** *14*, 100362.
11. Nicollet, C.; Flura, A.; Vibhu, V.; Rougier, A.; Bassat, J.-M.; Grenier, J.-C., An innovative efficient oxygen electrode for SOFC: Pr6O11 infiltrated into Gd-doped ceria backbone. *international journal of hydrogen energy* **2016,** *41* (34), 15538-15544.
12. Lei, L.; Tao, Z.; Hong, T.; Wang, X.; Chen, F., A highly active hybrid catalyst modified (La0.60Sr0.40)0.95Co0.20Fe0.80O3-δ cathode for proton conducting solid oxide fuel cells. *Journal of Power Sources* **2018,** *389*, 1-7.
13. Dogdibegovic, E.; Wang, R.; Lau, G. Y.; Tucker, M. C., High performance metal-supported solid oxide fuel cells with infiltrated electrodes. *Journal of Power Sources* **2019,** *410-411*, 91-98.
14. Park, B.-K.; Barnett, S. A., Boosting solid oxide fuel cell performance via electrolyte thickness reduction and cathode infiltration. *Journal of Materials Chemistry A* **2020,** *8* (23), 11626-11631.
15. Izuki, M.; Brito, M. E.; Yamaji, K.; Kishimoto, H.; Cho, D.-H.; Shimonosono, T.; Horita, T.; Yokokawa, H., Interfacial stability and cation diffusion across the LSCF/GDC interface. *Journal of Power Sources* **2011,** *196* (17), 7232-7236.

16. Dogdibegovic, E.; Templeton, J.; Yan, J.; Stevenson, J.; Zhou, X.-D., Compatibility of Praseodymium Nickelates with Various Cathode Current Collectors and Electrolytes. *ECS Transactions* **2013,** *57* (1), 1761.
17. De Vero, J. C.; Develos-Bagarinao, K.; Matsuda, H.; Kishimoto, H.; Ishiyama, T.; Yamaji, K.; Horita, T.; Yokokawa, H., Sr and Zr transport in PLD-grown Gd-doped ceria interlayers. *Solid State Ionics* **2018,** *314*, 165-171.
18. Hansen, K. K.; Menon, M.; Knudsen, J.; Bonanos, N.; Mogensen, M., The effect of a CGO barrier layer on the performance of LSM/YSZ SOFC cathodes. *Journal of The Electrochemical Society* **2010,** *157* (3), B309-B313.
19. Lu, Z.; Zhou, X.-D.; Templeton, J.; Stevenson, J. W., Electrochemical performance and stability of the cathode for solid oxide fuel cells IV. On the ohmic loss in anode-supported button cells with LSM or LSCF cathodes. *Journal of The Electrochemical Society* **2010,** *157* (6), B964-B969.
20. Dogdibegovic, E.; Alabri, N. S.; Wright, C. J.; Hardy, J. S.; Coyle, C. A.; Horlick, S. A.; Guan, W.; Stevenson, J. W.; Zhou, X.-D., Activity and Stability of (Pr1-xNdx)2NiO4 as Cathodes for Solid Oxide Fuel Cells: Part V. In Situ Studies of Phase Evolution. *Journal of The Electrochemical Society* **2017,** *164* (12), F1115-F1121.
21. Lübke, S.; Wiemhöfer, H. D., Electronic conductivity of Gd-doped ceria with additional Pr-doping1Dedicated to Prof. Dr. Bernt Krebs on the occasion of his 60th birthday.1. *Solid State Ionics* **1999,** *117* (3), 229-243.
22. Yamamoto, O., Solid oxide fuel cells: fundamental aspects and prospects. *Electrochimica Acta* **2000,** *45* (15-16), 2423-2435.
23. Ramesh, S.; Raju, K. J., Preparation and characterization of Ce1− x (Gd0. 5Pr0. 5) xO2 electrolyte for IT-SOFCs. *international journal of hydrogen energy* **2012,** *37* (13), 10311-10317.
24. Dogdibegovic, E.; Alabri, N. S.; Wright, C. J.; Hardy, J. S.; Coyle, C. A.; Horlick, S. A.; Guan, W.; Stevenson, J. W.; Zhou, X.-D., Activity and Stability of (Pr1-xNdx) 2NiO4 as Cathodes for Solid Oxide Fuel Cells: Part V. In Situ Studies of Phase Evolution. *Journal of the Electrochemical Society* **2017,** *164* (12), F1115.
25. Dogdibegovic, E.; Alabri, N. S.; Tenny, K.; Wright, C. J.; Hardy, J. S.; Coyle, C. A.; Horlick, S.; Guan, W.; Stevenson, J. W.; Zhou, X.-D., The role of interlayer on the catalytic activity and performance stability of (Pr1-xNdx) 2NiO4 as cathodes for solid oxide fuel cells. *ECS Transactions* **2017,** *78* (1), 983.
26. Dogdibegovic, E. Structural, interfacial, and electrochemical properties of Pr 2 NiO 4+ δ-based electrodes for solid oxide fuel cells. University of South Carolina, 2017.
27. Zhou, X. D.; Huebner, W.; Anderson, H. U., Processing of Nanometer-Scale CeO2 Particles. *Chemistry of Materials* **2003,** *15* (2), 378-382.
28. Dogdibegovic, E.; Wright, C. J.; Zhou, X.-D., Stability and Activity of (Pr1-xNdx)2NiO4 as Cathodes for Solid Oxide Fuel Cells: I. Quantification of Phase Evolution in Pr2NiO4. *Journal of the American Ceramic Society* **2016,** *99* (8), 2737-2741.
29. Chiba, R.; Taguchi, H.; Komatsu, T.; Orui, H.; Nozawa, K.; Arai, H., High temperature properties of Ce1-xPrxO2-δ as an active layer material for SOFC cathodes. *Solid State Ionics* **2011,** *197* (1), 42-48.
30. Schönleber, M.; Klotz, D.; Ivers-Tiffée, E., A Method for Improving the Robustness of linear Kramers-Kronig Validity Tests. *Electrochimica Acta* **2014,** *131*, 20-27.

31. Wan, T. H.; Saccoccio, M.; Chen, C.; Ciucci, F., Influence of the discretization methods on the distribution of relaxation times deconvolution: implementing radial basis functions with DRTtools. *Electrochimica Acta* **2015,** *184*, 483-499.
32. Ivers, T.; Eacute; E, E.; Weber, A.; eacute, Evaluation of electrochemical impedance spectra by the distribution of relaxation times. *Journal of the Ceramic Society of Japan* **2017,** *125* (4), 193-201.
33. Leonide, A.; Sonn, V.; Weber, A.; Ivers-Tiffée, E., Evaluation and modeling of the cell resistance in anode-supported solid oxide fuel cells. *Journal of The Electrochemical Society* **2007,** *155* (1), B36.
34. Hong, J.; Bhardwaj, A.; Bae, H.; Kim, I.-h.; Song, S.-J., Electrochemical Impedance Analysis of SOFC with Transmission Line Model Using Distribution of Relaxation Times (DRT). *Journal of The Electrochemical Society* **2020,** *167* (11), 114504.
35. Leonide, A. SOFC modelling and parameter identification by means of impedance spectroscopy. Ph.D. thesis, 2010.
36. Sumi, H.; Shimada, H.; Yamaguchi, Y.; Yamaguchi, T.; Fujishiro, Y., Degradation evaluation by distribution of relaxation times analysis for microtubular solid oxide fuel cells. *Electrochimica Acta* **2020,** *339*, 135913.
37. Lenser, C.; Gunkel, F.; Sohn, Y. J.; Menzler, N. H., Impact of defect chemistry on cathode performance: A case study of Pr-doped ceria. *Solid State Ionics* **2018,** *314*, 204-211.
38. Dogdibegovic, E. Structural, Interfacial, and Electrochemical Properties of $Pr_2NiO_{4+\delta}$ – Based Electrodes for Solid Oxide Fuel Cells. University of South Carolina, 2017.
39. E. Dogdibegovic, Q. C., N. S. Alabri, W. Guan, and X.-D. Zhou, Activity and Stability of (Pr1-xNdx)2NiO4 as Cathodes for Solid Oxide Fuel Cells: III Crystal Structure, Electrical Properties, and Microstructural Analysis. *Submitted to Journal of The Electrochemical Society* **2016**.
40. Boehm, E.; Bassat, J. M.; Dordor, P.; Mauvy, F.; Grenier, J. C.; Stevens, P., Oxygen diffusion and transport properties in non-stoichiometric Ln(2-x)NiO(4+delta) oxides. *Solid State Ion.* **2005,** *176* (37-38), 2717-2725.
41. Broux, T., *Dalton Trans.* **2016,** *45*, 3024-3033.
42. Lübke, S.; Wiemhöfer, H.-D., Electronic conductivity of Gd-doped ceria with additional Pr-doping. *Solid State Ion.* **1999,** *117* (3-4), 229-243.
43. Dogdibegovic, E.; Alabri, N. S.; Tenny, K.; Wright, C. J.; Hardy, J. S.; Coyle, C. A.; Horlick, S.; Guan, W.; Stevenson, J. W.; Zhou, X.-D., The Role of Interlayer on the Catalytic Activity and Performance Stability of (Pr1-xNdx)2NiO4as Cathodes for Solid Oxide Fuel Cells. *ECS Transactions* **2017,** *78* (1), 983-992.
44. Dogdibegovic, E.; Cai, Q.; Alabri, N. S.; Guan, W.; Zhou, X.-D., Activity and Stability of (Pr1-xNdx) 2NiO4 as Cathodes for Solid Oxide Fuel Cells. *Journal of The Electrochemical Society* **2016,** *164* (2), F99.
45. Zhang, Y.; Wang, W.; Wang, Y.; Xu, N.; Tian, G.; Karsili, T. N.; Yang, J.; Zhou, X. D., Role of Pr-Vacancies and O-Interstitials on the Activity and Stability of (Pr1− xLnx) 2NiO4 (Ln= La, Nd, Pm, Sm, Gd, Tb, Dy, and Ho) towards Oxygen Reduction Reactions: A DFT Study. *Journal of The Electrochemical Society* **2021,** *168* (12), 124508.
46. Kjelstrup, S.; Bedeaux, D., *Non-equilibrium thermodynamics of heterogeneous systems*. World Scientific: 2008.
47. Virkar, A. V., Theoretical analysis of the role of interfaces in transport through oxygen ion and electron conducting membranes. *Journal of Power Sources* **2005,** *147* (1), 8-31.

48. Dreyer, W.; Guhlke, C.; Müller, R., A new perspective on the electron transfer: recovering the Butler–Volmer equation in non-equilibrium thermodynamics. *Physical Chemistry Chemical Physics* **2016,** *18* (36), 24966-24983.
49. Bazant, M. Z., Theory of Chemical Kinetics and Charge Transfer based on Nonequilibrium Thermodynamics. *Accounts of Chemical Research* **2013,** *46* (5), 1144-1160.
50. Gedik, A.; Lubos, N.; Kabelac, S., Coupled Transport Effects in Solid Oxide Fuel Cell Modeling. *Entropy* **2022,** *24* (2), 224.
51. Virkar, A. V., A model for solid oxide fuel cell (SOFC) stack degradation. *Journal of Power Sources* **2007,** *172* (2), 713-724.
52. Ferguson, T. R. Lithium-ion battery modeling using non-equilibrium thermodynamics. Massachusetts Institute of Technology, 2014.
53. Hua, X.; Allan, P. K.; Gong, C.; Chater, P. A.; Schmidt, E. M.; Geddes, H. S.; Robertson, A. W.; Bruce, P. G.; Goodwin, A. L., Non-equilibrium metal oxides via reconversion chemistry in lithium-ion batteries. *Nature communications* **2021,** *12* (1), 1-11.
54. Virkar, A. V., A model for degradation of electrochemical devices based on linear non-equilibrium thermodynamics and its application to lithium ion batteries. *Journal of Power Sources* **2011,** *196* (14), 5970-5984.
55. Virkar, A. V., Mechanism of oxygen electrode delamination in solid oxide electrolyzer cells. *International Journal of Hydrogen Energy* **2010,** *35* (18), 9527-9543.
56. Virkar, A., Failure of ion-conducting materials by internal precipitation under electrolytic conditions. *Engineered Ceramics: Current Status and Future Prospects; Ohji, T., Singh, M., Eds* **2016**, 59-76.
57. Williams, N. J.; Seymour, I. D.; Leah, R. T.; Banerjee, A.; Mukerjee, S.; Skinner, S. J., Non-equilibrium thermodynamics of mixed ionic-electronic conductive electrodes and their interfaces: a Ni/CGO study. *Journal of Materials Chemistry A* **2022,** *10* (20), 11121-11130.
58. Mistry, A. N.; Cano-Banda, F.; Law, D.; Hernandez-Guerrero, A.; Mukherjee, P. P., Non-equilibrium thermodynamics in electrochemical complexation of Li–oxygen porous electrodes. *Journal of Materials Chemistry A* **2019,** *7* (15), 8882-8888.
59. Mao, Z.-Y.; Sun, Y.-P.; Scott, K., Evaluation of apparent lithium-ion diffusion coefficients in FePO4/LiFePO4 cathode material particles from linear non-equilibrium thermodynamics and principle of electroneutrality. *Journal of Electroanalytical Chemistry* **2016,** *766*, 107-119.